Multi-resolution reconstruction of spectral images from compressed measurements by single pixel optical sensing architecture

Author
HANS YECID GARCIA ARENAS

UNIVERSIDAD INDUSTRIAL DE SANTANDER
FACULTAD DE INGENIERÍAS FISICOMECÁNICAS
ESCUELA DE INGENIERÍAS ELÉCTRICA, ELECTRÓNICA Y TELECOMUNICACIONES
MAESTRÍA EN INGENIERÍA ELECTRÓNICA
BUCARAMANGA

2018

Multi-resolution reconstruction of spectral images from compressed measurements by single pixel optical sensing architecture

Author

HANS YECID GARCIA ARENAS

In fulfillment of the requirements for the degree of **Magíster en ingeniería electrónica**

Director
Henry Arguello Fuentes
Ph.D. Electrical and Computer Engineering
Universidad Industrial de Santander

Co-director
Claudia V. Correa Pugliese
Ph.D. Electrical and Computer Engineering
University of Delaware

UNIVERSIDAD INDUSTRIAL DE SANTANDER
FACULTAD DE INGENIERÍAS FISICOMECÁNICAS
ESCUELA DE INGENIERÍAS ELÉCTRICA, ELECTRÓNICA Y TELECOMUNICACIONES
MAESTRÍA EN INGENIERÍA ELECTRÓNICA
BUCARAMANGA
2018

Contents

List of Figures

Abstract

Title: Multi-resolution reconstruction of spectral images from compressed measurements by single pixel optical sensing architecture

Author: Hans Yecid Garcia Arenas

Keywords: Multi-resolution, super-pixel, single pixel camera, compressive spectral imaging.

Spectral imaging is used in a wide range of applications for non-invasive detection and classification. However, the massive amount of involved data increases its processing and storing costs. In contrast, compressive spectral imaging (CSI) establishes that the three-dimensional spectral data cube can be recovered from a small set of projections that are generally captured in 2-dimensional detectors. Furthermore, the single-pixel camera (SPC) has been also employed for spectral imaging. Specifically, SPC captures the spatial and spectral information in a single measurement. CSI reconstructions are traditionally obtained by solving a minimization problem using iterative algorithms. However, the computational load of these algorithms is high due to the dimensionality of the involved sensing matrices. In this work, a Multi-resolution (MR) reconstruction model is proposed such that the complexity of the inverse problem can be reduced by grouping pixels with spectral similarities from an initial fast-low-resolution reconstruction of the scene.

[1]Research work

[2]Escuela de ingenierías eléctrica, electrónica y telecomunicaciones, Universidad Industrial de Santander. Director, Henry Arguello Fuentes. Co-director, Claudia V. Correa Pugliese

Introduction

Spectral imagery (SI) consists on three-dimensional data sets with two spatial dimensions (x, y), and one dimension in the spectral domain λ. This type of images is useful in a wide range of applications such as ground-cover classification, mineral exploration, and agricultural assessment in remote sensing [6], biomedical imaging [7], identification of military objectives [8] and others. These applications often require high-resolution images to discriminate between specific details of the scene, which increases the cost of processing and storing due to the massive amount of involved data. On the other hand, compressive sensing (CS) principles have been recently applied to SI acquisition [9, 10], in a field called compressive spectral imaging (CSI). Specifically, CSI establishes that it is possible to retrieve the spatial and spectral information of a scene from a small number of projections, that are generally captured in 2-dimensional detectors. Furthermore, the single-pixel camera (SPC) has been also employed for spectral imaging [11], which captures the three-dimensional source in a single measurement. The use of SPC helps in reducing the general acquisition costs related to hardware fabrication. CSI reconstructions are traditionally obtained by solving a minimization problem using iterative algorithms and the acquired measurements. However, the reconstruction complexity increases in proportion to the image resolution. Approaches to alleviate the computational load in compressive spectral imaging reconstructions rely on separable sensing operators [12], hardware implementations such as GPU and FPGA [13], and block reconstructions [14]. All of the aforementioned reconstruction schemes recover the three-dimensional source without exploiting specific characteristics of the scene different to the sparsity constraint. This work proposes to take advantage of spectral similarities between spatial pixels of the scene, such that they can be grouped into "super-pixels". In this way, the dimensionality of the associated sensing matrix can be reduced and a multi-resolution version of the scene can be recovered.

Chapter 1

Objectives

1.1 General

To design a reconstruction methodology for multi-resolution spectral imaging from compressed measurements acquired with a single pixel optical architecture.

1.2 Specifics

- To develop a mathematical description of the compressive spectral imaging acquisition process in a single pixel camera.
- To develop a mathematical description of the inverse problem to recover the high-resolution spectral signals measured by single pixel architecture.
- To develop the mathematical model for the multi-resolution reconstruction process from single pixel camera measurements.
- To simulate and analyze the performance of the multi-resolution reconstruction model with respect to the full-resolution reconstruction approach.
- To test the performance of the proposed multi-resolution approach on real data captured from a testbed implementation of the single pixel optical architecture.

Chapter 2

Theoretical Background

2.1 Spectral Imaging (SI)

Spectral imagery is composed of two spatial dimensions (x, y), and one dimension in the wavelength domain λ. Thus, the spectral bands are the intensities at each λ at which the object is measured. Depending on the range of analyzed wavelengths, spectral images can be classified as ultraviolet (UV) (200-380nm), visible (380-780nm) or infrared (IF) (780nm-50000nm). These images differ from the traditional gray scale images in that each spatial point contains a complete spectrum instead of just an intensity value [15]. In the RGB case, three different spectral channels compose the image: red, green and blue. Furthermore, the amount of measured bands is used to classify SI as: multi-spectral images that contain tens of bands, or hyper-spectral images that refer to those with up to hundreds of bands. The information contained in SI makes them applicable to several areas such as ground-cover classification, mineral exploration, and agricultural assessment in remote sensing [6]; biomedical imaging [7] for which SI offer great potential for noninvasive disease diagnosis and surgical guidance; identification of military objectives in surveillance and security applications [8] among others.

There are several methods for acquiring a spectral image, and a common characteristic of many of these methods is that they require scanning the area of interest as illustrated in Fig. 1. For instance, an approach that captures the spectrum for a single point is called Whisk-broom spectrometer [16]; another approach, known as filtered camera acquires all the spatial pixels for each wavelength at a time [5]; on the other hand, the push-broom spectrometer measures the spectrum across a spatial line and then scans the scene across the remaining spatial dimension [17]. All of the aforementioned methods require acquiring a massive amount of data, given that they rely on the Nyquist-Shannon theorem [18, 19]. In addition, they experience low sensing speed and high complexity for processing and storage.

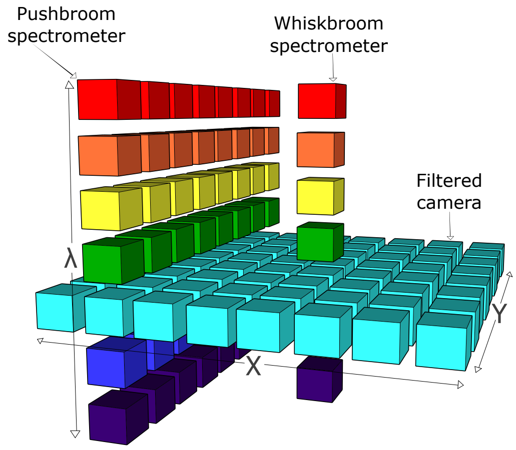

Figure 1: Scanning spectral imaging approaches for a spectral data cube with X and Y as spatial coordinates and λ the wavelengths.

2.2 Compressive Sensing(CS) for SI

An alternative sampling theory called compressed sensing (CS) proposes to perform compression and sampling in a single process[9, 10, 20]. Specifically, CS establishes that it is possible to retrieve a signal from a small number of samples under some given conditions. This technique is based on the assumption that the signal under analysis has a sparse representation in a basis $\mathbf{\Psi}$. In particular, a spectral image $\mathbf{f} \in \mathbb{R}^{MNL}$ has a dispersion level S, if it can be represented as a linear combination of S vectors on any basis $\mathbf{\Psi}$, such that $\mathbf{f} = \mathbf{\Psi}\boldsymbol{\theta}$ with $S \ll MNL$. Thus, instead of acquiring MNL samples (voxels), CS captures $k \ll NML$ random projections of the scene. The sensing process can be represented in matrix form as $\mathbf{g} = \mathbf{Hf}$, where $\mathbf{H}$ is the matrix that represents the transfer function of the acquisition system[21]. Because the number of measurements is considerably smaller than the number of voxels, the inverse problem given by $\hat{\mathbf{f}} = \mathbf{H}^{-1}\mathbf{g}$, is ill conditioned, and leads to an infinite number of solutions. Therefore, reconstruction of the signal $\mathbf{f}$ is obtained using compressed sensing optimization algorithms that take advantage of the sparse representation of $\mathbf{f}$ in the transformation basis $\mathbf{\Psi}$. Specifically, these algorithms obtain an approximation of $\boldsymbol{\theta}$ with the optimization problem given by

$$\hat{\mathbf{f}} = \mathbf{\Psi}\{argmin_{\theta}\left(||\mathbf{H}\mathbf{\Psi}\boldsymbol{\theta} - \mathbf{g}||_2^2 + \tau||\boldsymbol{\theta}||_1\right)\}, \tag{1}$$

where τ is a regularization parameter.

In recent years, different optical architectures have been developed to implement the compressive sampling theory for the acquisition of spectral images, which has been termed as compressive spectral imaging (CSI). Figure 2 shows some of the most representative compressive spectral imaging architectures: SSCSI, CASSI, DCSI, PMVIS and SPC. The Spatial-Spectral Encoded Compressive HS Imager (SSCSI) is built by combining optical spatial and spectral modulation, which provides a high degree of randomness in the measured projections, and the sparsity-constrained reconstruction algorithm[1]; the coded aperture snapshot spectral imager (CASSI) uses a coded aperture and one or more dispersive elements to modulate the optical field from a scene while a detector captures a 2-dimensional, multiplexed projection of the three-dimensional data cube representing the scene [2]; the dual-coded hyper-spectral imager (DCSI) separately encodes both spatial and spectral dimensions within a single exposure, achieving an independent spectral code for each sensor pixel, DCSI facilitates flexible capture modes customized for different applications[3]; the prism-mask multispectral video imaging system (PMVIS) is composed of an occlusion mask, a prism, and a grayscale camera, the radiance from the scene is sampled by the occlusion mask to avoid overlap among spectra on the image plane, spatial and angular smoothness in reflectance is assumed for each captured scene point, so that the light rays sampled by a mask hole have the same radiance[4]; the single pixel camera (SPC) which is an optical device comprising a digital micromirror device (DMD), two lenses, a single photon detector, and an analog-to-digital (A/D) converter, computes random linear measurements of the scene under view in a single measure[5]. Each of these architectures presents its own advantages and drawbacks for different applications. However, most of them require two dimensional sensors, while SPC uses a single pixel detector, which provides realiable spectral images with a low cost hardware. Thus, this work focuses on the SPC, which is further described in chapter 4.

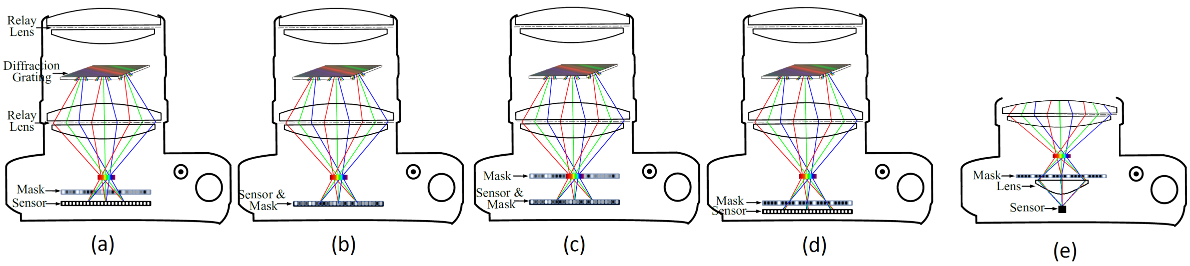

Figure 2: Most representative CSI optical architectures (a) Coded Mask (SSCSI) [1], (b) Coded Aperture CASSI [2], (c)Dual Coded Mask DCSI [3], (d) Prism and Mask PMVIS [4] and (e) SPC [5]. Source:[1]

2.3 Multi-resolution Images

A Multi-resolution image is a recent approach which assumes blocks of pixels with similar characteristics that can be grouped into a "super-pixel", such that the number of elements in the full image is reduced [22]. The concept was first introduced by the recommendation H.265: High-efficiency video coding [23], and VP9 [24] developed by Google, which uses blocks of pixels with different size to reduce the amount of storage needed. Both approaches can be used with high-definition video (UHD), but they were designed for post-processing video based on the Nyquist-Shannon theorem. Later, in [25, 26] the multiresolution concept was introduced for grayscale images using compressed sensing. More specifically, in the reconstruction process of [25], image pixels are classifies as background or region of interest, using prior information of the location of objects of interest. Then, the background is recovered at a lower resolution and the region of interest at higher resolutions. On the other hand, in [26] the image is recovered at a different resolution from that of the original, using a compressed sensing set of projections. A first approximation of a multi-resolution reconstruction method for spectral images using CS was presented in [27], which reconstructs the SI for the background and the region of interest in two different minimization problems with low and high resolution, respectively, at the expense of high computational cost. To the best of our knowledge, a computationally efficient multi-resolution reconstruction method for compressive spectral imaging has not yet been developed.

Chapter 3

SPC Sensing and Multi-Resolution Reconstruction Models

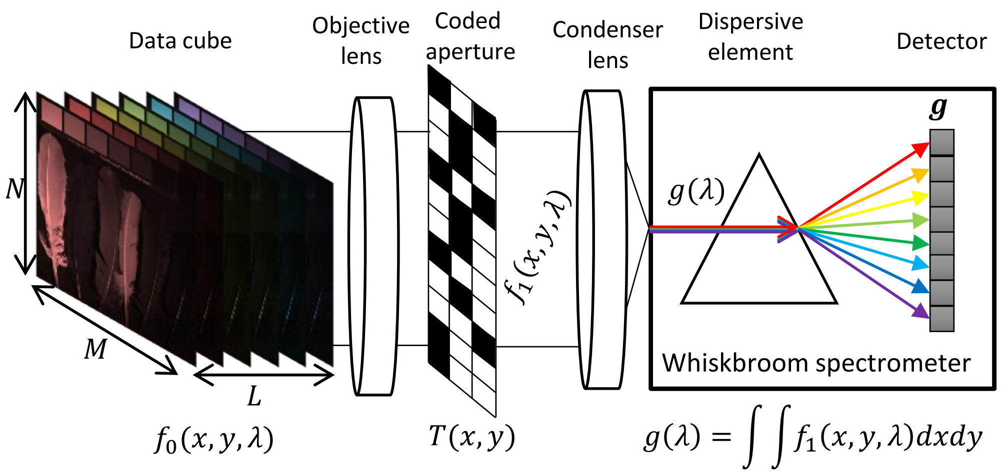

Figure 3: Single pixel camera (SPC) sensing phenomenon for spectral imaging.

The multi-resolution reconstruction approach proposed in this work is based on the compressive spectral measurements acquired with the SPC, whose sensing process is illustrated in Fig. 3. This optical architecture is composed by an objective lens, a coded aperture $T(x, y)$, with x, y the spatial coordinates, a condenser lens and a single pixel detector. Specifically, the objective lens focuses the input scene $f_0(x, y, \lambda)$ onto the coded aperture that spatially modulates all the spectral components of the object. The coded aperture is a binary pattern that either blocks the light o lets it pass through at each spatial point (x, y). In this case, the modulation consists of a Hadamard pattern with entries 1 or -1. In practical terms, the modulation effect caused by the -1 entries can be implemented using an all-ones coded aperture measurement and subtract it from each captured snapshot. Mathematically, the coded aperture effect is represented as

$$f_1(x, y, \lambda) = f_0(x, y, \lambda)T(x, y). \tag{2}$$

The spatially modulated scene is then concentrated in a single point by a condenser lens, where it is captured by a single pixel sensor. Specifically, a single point Whisk-broom spectrometer is used as a detector such that all the incoming modulated spectral source is captured in a single measurement as a function of λ. The spatially condensed coded scene is given by

$$g(\lambda) = \int\int f_1(x, y, \lambda)dxdy. \tag{3}$$

The acquired spectrum is discretized by the spectrometer according to the pixel pitch of the detector Δ_e. This process can be mathematically expressed as

$$g_l = \int_{\Lambda_l} g(\lambda)rect\left(\frac{\lambda}{\Delta_e} - l\right) d\lambda, \tag{4}$$

where $\Lambda_l = \{\lambda | \Delta_e(l-1)/2 \leq \lambda \leq \Delta_e(l+1)/2\}$ represents the set of wavelengths that are captured within the l-th spectral band. Using the discrete measurements g_l, a discrete sensing model of the system can be developed. Let $\mathbf{F} \in \mathbb{R}^{M \times N \times L}$ be the discrete SI, where M and N are the spatial dimensions, L is the number of spectral bands. The coded aperture can be represented in discrete form as $\mathbf{T} \in \mathbb{R}^{M \times N}$ which is given by

$$T(x, y) = \sum_{i,j} \mathbf{T}_{(i,j)} rect\left(\frac{x}{\Delta_c} - i, \frac{y}{\Delta_c} - j\right), \tag{5}$$

for $i = 1, \ldots, M$ and $j = 1, \ldots, N$, where $M \times N$ is the spatial resolution of the coded aperture, and Δ_c is the pixel size of the coded aperture. Then the discrete sensing process is given by

$$g_l = \sum_i \sum_j \mathbf{F}_{(i,j,l)} \mathbf{T}_{(i,j)}, \tag{6}$$

which can be rewritten in matrix form as

$$g_l = \mathbf{h}^T \mathbf{f}_l, \tag{7}$$

for $l = 1, 2, \ldots, L$, where $\mathbf{h}$ is a vector form of $\mathbf{T}$ given by $\mathbf{h} = [T_{1,1}, T_{2,1}, \cdots, T_{M,N}]$, and $\mathbf{f}_l$ is a vector form of the l-th spectral band of $\mathbf{F}$. Furthermore, each captured snapshot employs a different coded aperture pattern $\mathbf{T}^k$. Several shots can be stacked in a single vector as

$\mathbf{g}_l = [g_l^1, \ldots, g_l^k]^T$. Then, the multi-shot sensing model for each band is given by

$$\mathbf{g}_l = \mathbf{H}\mathbf{f}_l, \tag{8}$$

where $\mathbf{H}$ is a $K \times MN$ matrix, K is the number of shots, each row of $\mathbf{H} = [\mathbf{h}_1^T, \ldots, \mathbf{h}_K^T]$ is the vector form of the coded aperture used on that particular shot. In general, the sensing model for all bands can be written as

$$\mathbf{g} = \hat{\mathbf{H}}\mathbf{f}, \tag{9}$$

where $\hat{\mathbf{H}}$ is the block diagonal sensing matrix obtained as

$$\hat{\mathbf{H}} = \begin{pmatrix} \mathbf{H} & \mathbf{0} & \cdots & \mathbf{0} \\ \mathbf{0} & \mathbf{H} & \cdots & \mathbf{0} \\ \vdots & \vdots & \ddots & \vdots \\ \mathbf{0} & \mathbf{0} & \cdots & \mathbf{H} \end{pmatrix}, \tag{10}$$

$\mathbf{f} = \left[(\mathbf{f}_1)^T, \cdots, (\mathbf{f}_L)^T\right]^T$, and $\mathbf{g} = \left[(\mathbf{g}_1)^T, \cdots, (\mathbf{g}_L)^T\right]^T$. Furthermore, the compression ratio in this model is given by $\gamma = \frac{K}{MN}$, where $\gamma \in [0, 1]$. An example of $\hat{\mathbf{H}}$ using a random binary matrix $\mathbf{T}$ is illustrated in Fig. 4, for $M = 4$, $N = 4$, $L = 4$ and $\gamma = 0.25$.

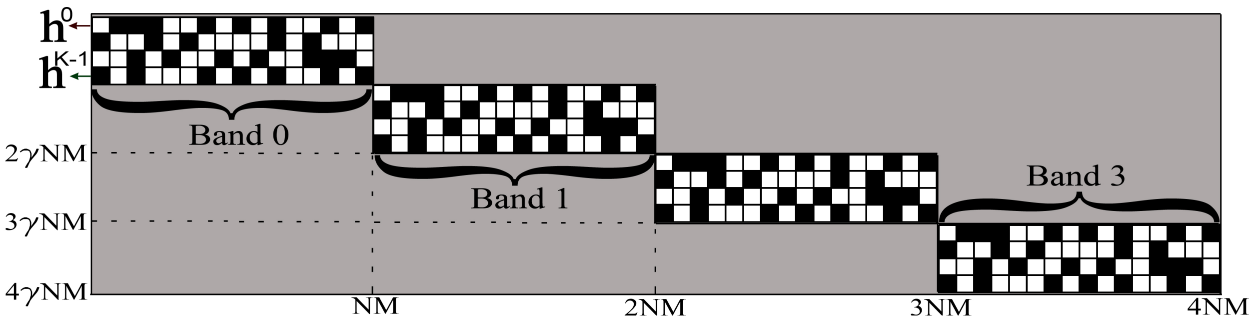

Figure 4: Example of SPC sensing matrix $\hat{\mathbf{H}}$ for $N = 4$, $M = 4$, $\gamma = 0.25$ and $L = 4$. White squares represent 1, black squares represent -1 and gray zones are 0.

Reconstructions from SPC measurements can be obtained by solving Eq. 1. To date, several optimization algorithms have been developed to find a solution for the inverse CSI problem. In general, these algorithms work under the sparsity assumption of the underlying signal and their computational load is high due to the high dimensionality of the sensing matrices and the signal itself.

Therefore, this work presents a reconstruction scheme that assumes that pixels of the same class have the same spectrum, such that they can be grouped into super-pixels, which reduces the amount of unknowns to recover in the inverse problem. Thus, the complexity of the resulting reconstruction problem is drastically reduced. Specifically, this work takes advantage of the spectral similarities of the pixels in the image. Given that, the scenes under analysis exhibit highly correlated areas in which several pixels can be grouped into super-pixels without losing information or inducing considerable errors, this correlation can be measured with the MSE between the spectral response of each pixel with the mean of the all pixels into the super-pixel. Figure 5 summarizes the proposed reconstruction scheme, in which a fast low resolution (LR) reconstruction of the scene $\boldsymbol{\beta}$ is first obtained; then, a full resolution version of the image $\bar{\mathbf{f}}$ is attained by interpolating the LR reconstruction which is used to generate a multi-resolution (MR) map of super-pixels $\hat{\mathbf{D}}$, taking into account their spectral signatures. This map of super-pixels allows the definition of a decimation matrix that relates the full-resolution spectral image with its MR version. The associated multi-resolution decimation matrix $\hat{\mathbf{D}}$ is used to modify the sensing matrix $\hat{\mathbf{H}}$, such that Eq. 1 is solved with $\hat{\mathbf{H}}\hat{\mathbf{D}}^T$ as the sensing matrix instead of just $\hat{\mathbf{H}}$, this modification consists of grouping the spatial pixels with close spectral signature into a super-pixel with the average of these spectral signatures. Next, each step from Fig. 5 is described in detail.

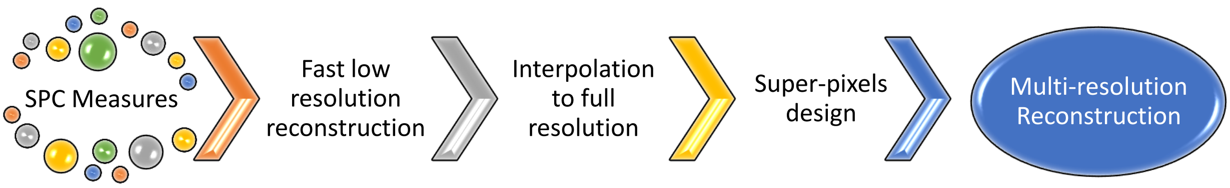

Figure 5: Proposed multi-resolution (MR) reconstruction process.

In order to obtain the fast LR approximation of the spectral scene, let the matrix $\mathbf{H}$ be designed as in [28]

$$\mathbf{H} = \mathbf{W}\mathbf{D} + \mathbf{Z}, \tag{11}$$

where $\mathbf{W}$ is a $\gamma MN \times \gamma MN$ Hadamard matrix, $\mathbf{D}$ is a decimation matrix and $\mathbf{Z}$ is a $\gamma MN \times MN$ auxiliary binary matrix that improves the CS properties of $\mathbf{H}$, such as the condition number. Furthermore, this matrix should guarantee that the values of $\mathbf{H}$ are only -1 or 1 for implementation purposes. The SPC sensing matrix, is then obtained as in Eq. 10. Based on Eq 11, a fast LR approximation of $\mathbf{F}$ can be attained by simply applying the inverse Hadamard transform to the measurements. Mathematically, using the structure of the sensing matrix for all spectral bands $\hat{\mathbf{H}}$, the LR approximation is obtained as

$$\boldsymbol{\beta} = \hat{\mathbf{W}}^T\mathbf{g}, \tag{12}$$

where $\hat{\mathbf{W}}$ is a block diagonal matrix that accounts for the inverse Hadamard transform applied to all spectral bands and is given by

$$\hat{\mathbf{W}} = \begin{pmatrix} \mathbf{W} & \mathbf{0} & \cdots & \mathbf{0} \\ \mathbf{0} & \mathbf{W} & \cdots & \mathbf{0} \\ \vdots & \vdots & \ddots & \vdots \\ \mathbf{0} & \mathbf{0} & \cdots & \mathbf{W} \end{pmatrix}. \tag{13}$$

Using the LR version of the scene, $\boldsymbol{\beta}$, a fast full-resolution (FR) approximation of $\mathbf{f}$ can be obtained by applying an up-sampling operator without using an iterative algorithm. This interpolated FR approximation is later used to generate a map of image super-pixels with respect to their spectra. Mathematically, the fast FR approximation of the scene is obtained as $\bar{\mathbf{f}} = \mathbf{U}\boldsymbol{\beta}$, where $\mathbf{U}$ is the employed up-sampling operator, such as a bilinear interpolation matrix. Using Eqs. 11 and 12, the interpolation of the l-th spectral band is given by

$$\begin{aligned} \bar{\mathbf{f}}_l &= \mathbf{U}\mathbf{W}^T(\mathbf{W}\mathbf{D} + \mathbf{Z})\mathbf{f}_l \\ &= \mathbf{U}\mathbf{W}^T(\mathbf{W}\mathbf{D})\mathbf{f}_l + \boldsymbol{\omega} \\ &= \mathbf{f}_l + \boldsymbol{\omega}, \end{aligned} \tag{14}$$

where $\boldsymbol{\omega} = \mathbf{U}\mathbf{W}^T\mathbf{Z}\mathbf{f}_l$. Given that $\mathbf{W}$ is a Hadamard matrix, and assuming that the upsampling and downsampling matrices satisfy $\mathbf{U}\mathbf{D} \approx \mathbf{I}$, where $\mathbf{I}$ is the identity matrix, $\boldsymbol{\omega}$ can be considered as noise induced by the $\mathbf{Z}$ matrix which is not taken account into for generating the MR super-pixels. The correlation between the spectral signatures of the pixels of $\bar{\mathbf{f}}$ in Eq. 14 determines the guidelines to group several pixels with similar spectral signatures into a superpixel. Assuming that $\mathbf{f} = \hat{\mathbf{D}}^T\boldsymbol{\xi}$, where $\hat{\mathbf{D}}$ is the MR downsampling matrix and $\boldsymbol{\xi}$ contains the spectral information of each super-pixel, an estimation of $\hat{\mathbf{D}}$ can be obtained using $\bar{\mathbf{f}}$. Specifically, $\hat{\mathbf{D}}$ is a diagonal matrix whose entries correspond to the downsampling matrix for each spectral band ($\boldsymbol{\Delta}$), and is expressed as

$$\hat{\mathbf{D}} = \begin{pmatrix} \boldsymbol{\Delta} & \mathbf{0} & \cdots & \mathbf{0} \\ \mathbf{0} & \boldsymbol{\Delta} & \cdots & \mathbf{0} \\ \vdots & \vdots & \ddots & \vdots \\ \mathbf{0} & \mathbf{0} & \cdots & \boldsymbol{\Delta} \end{pmatrix}. \tag{15}$$

Notice that several downsampling matrices can be employed. The procedure to generate the MR matrix $\boldsymbol{\Delta}$ is based on the analysis of the spectral signatures in the fast-full resolution reconstruction of the scene $\bar{\mathbf{f}}$. The main goal is to decompose the interpolated scene $\bar{\mathbf{F}}$ which is the $3D$ form of $\bar{\mathbf{f}}$ into subsets called super-pixels. Several methods for generating image super-pixels are available in the state of art, including graph-based, gradient accent, TurboPixels [29], quick super-pixels[30], and SLIC [31]. In particular, this work focuses on three main possibilities for $\boldsymbol{\Delta}$, based on SLIC algorithm[31], and two developed methods based on regular and irregular super-pixels. The procedure to generate the MR matrix $\hat{\mathbf{D}}$ is described in detail in Section 4.1 for the rectangular approach, in section 4.2 for the irregular approach and for the SLIC based super-pixels in section 4.3. Using $\hat{\mathbf{D}}$, $\hat{\mathbf{H}}$ and the measurements $\mathbf{g}$, super-pixels designed in the SI can be reconstructed by solving

$$\boldsymbol{\xi} = \boldsymbol{\Psi}\{argmin_{\theta}||\hat{\mathbf{H}}\hat{\mathbf{D}}^T\boldsymbol{\Psi}\boldsymbol{\theta} - \mathbf{g}||_2^2 + \tau||\boldsymbol{\theta}||_1\}, \tag{16}$$

where τ is a regularization parameter, $\boldsymbol{\Psi}$ is the sparse representation basis and $\hat{\mathbf{D}}$ is the down-sampling matrix that indicates the spatial positions in which the elements of $\boldsymbol{\xi}$ should be placed based on the associated map of super-pixels. It is worth noting that Eq. 16 is solved for the sensing matrix $\hat{\mathbf{H}}\hat{\mathbf{D}}^T$ which is the equivalent MR sensing matrix. Therefore, given the fact that the number of columns of $\hat{\mathbf{H}}\hat{\mathbf{D}}^T$ is less than or equal to those of $\hat{\mathbf{H}}$, the computational complexity of the MR problem in Eq. 16 is reduced with respect to the original problem in Eq. 1. Specifically, the complexity of the problem in Eq. 1 is $O(KNML)$, while the MR problem in Eq. 16 has complexity $O(KCL)$, where K is the number of measurements and $C \leq MN$ is the number of unknowns to recover i.e. super-pixels. The number of super-pixels C, depends on the method employed to design the MR decimation matrix, as it will be describe in the following sections. Using the solution of Eq. 16, the reconstructed data cube $\hat{\mathbf{f}}$ can then be obtained as

$$\hat{\mathbf{f}} = \hat{\mathbf{D}}^T\boldsymbol{\xi}. \tag{17}$$

Algorithm 1 presents a summary of the proposed reconstruction methodology, whose process is illustrated in Fig. 6.

Algorithm 1 Algorithm for recovering a multi-resolution spectral image

1: **Input:** Compressive measurements $\mathbf{g}$
2: **Output:** MR SI $\hat{\mathbf{f}}$
3: Reconstruct fast LR image $\boldsymbol{\beta} = \hat{\mathbf{W}}^T\mathbf{g}$
4: Interpolate fast full resolution image $\bar{\mathbf{f}} = \mathbf{U}\boldsymbol{\beta}$
5: Build $\hat{\mathbf{D}}$ using $\boldsymbol{\Delta}$ that is designed using Algorithm 2 or 3
6: Recover super-pixels $\boldsymbol{\xi} = \boldsymbol{\Psi}\{argmin_{\theta}||\hat{\mathbf{H}}\hat{\mathbf{D}}^T\boldsymbol{\Psi}\boldsymbol{\theta} - \mathbf{g}||_2^2 + \tau||\boldsymbol{\theta}||_1\}$
7: Rearrange the MR SI as $\hat{\mathbf{f}} = \hat{\mathbf{D}}^T\boldsymbol{\xi}$

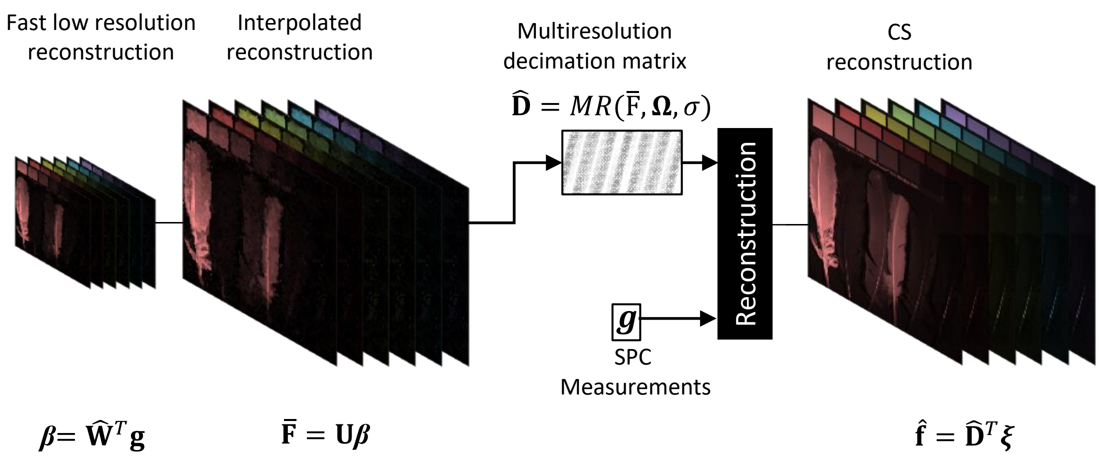

Figure 6: Proposed multi-resolution (MR) reconstruction process, notice that $\boldsymbol{\xi}$ is calculated solving the minimization problem in Eq. 16.

3.1 Design of Multi-resolution decimation matrix ($\mathbf{\Delta}$) for rectangular super-pixels

The construction of the MR matrix $\mathbf{\Delta}$ is based on the analysis of the spectral signatures in $\bar{\mathbf{f}}$ from Eq. 14 as presented in Algorithm 2. The main goal is to decompose each spectral band of the interpolated scene $\bar{\mathbf{F}}$, which is the 3D form of $\bar{\mathbf{f}}$, into subsets of rectangular super-pixels of size $2^\eta \times 2^\eta$, based on the inputs of the algorithm which are: the set of spatial coordinates of the image $\mathbf{\Omega}$; the error tolerance σ; the parameter for the super-pixels size η and the interpolated scene $\bar{\mathbf{F}}$. The super-pixel size varies within the set $\mathbf{S} = [2^\eta, 2^{\eta-1}, \dots, 1]$ which is indexed by the variable z, starting at $z = 0$ as in line 3. The proposed method, as shown in line 7, chooses a random point $(\hat{\imath}, \hat{\jmath})$ and creates the set $\mathbf{B}$ that contains the spatial coordinates of a $2^\eta \times 2^\eta$ super-pixel whose top-left corner is the point $(\hat{\imath}, \hat{\jmath})$. Therefore, the actual super-pixel is denoted as $\bar{\mathbf{F}}_\mathbf{B}$. Then, in line 9, Algorithm 2 calculates the average normalized spectrum of $\bar{\mathbf{F}}_\mathbf{B}$ as $\mathbf{p} = E\{\bar{\mathbf{F}}_\mathbf{B}\}$, in order to determine the spectral similarity between each point from the super-pixel $\bar{\mathbf{F}}_\mathbf{B}$ and $\mathbf{p}$. In this work, the selected criterion to measure the spectral similarity is the Mean Squared Error (MSE). In line 10, if the maximum MSE is smaller than the fixed threshold σ then, the spatial points in $\mathbf{B}$ are grouped into a single superpixel as in lines 11 to 16. Otherwise,the super-pixel $\bar{\mathbf{F}}_\mathbf{B}$ cannot be created. Consider the case in which the threshold criterion in line 10 is satisfied, then the algorithm, in lines 11 and 12, creates $\mathbf{\Gamma} \in \mathbb{R}^{M \times N}$ which is an indicator matrix that accounts for the spatial coordinates of the pixels in the super-pixels and is given by

$$\mathbf{\Gamma}_{(i,j)} = \begin{cases} 1 & if \;\; max(MSE(\mathbf{p}, \bar{\mathbf{F}}_{\mathbf{B}})) < \sigma \; and \; (i,j) \in \mathbf{B} \\ 0 & otherwise \end{cases}. \quad (18)$$

In this case, the vector form of $\mathbf{\Gamma}$ is added as a new row of the MR decimation matrix $\mathbf{\Delta}$, as in line 13. Notice that all points in $\mathbf{B}$ can only belong to one super-pixel, then, the set of available points is updated by removing $\mathbf{B}$ from $\mathbf{\Omega}$ as in line 15.

On the other hand, when the threshold criterion is not satisfied and the super-pixel cannot be constructed, the point $(\hat{i}, \hat{j})$ cannot be the top-left corner of any other super-pixel of the same size, however it can be included on another super-pixel of any size. Indeed, the point $(\hat{i}, \hat{j})$ can be the top-left corner of a smaller super-pixel. Therefore, this results in two different types of points: the ones available to be assigned to future super-pixels which are referred to as $\mathbf{\Omega}$, and the ones eligible to be analyzed as top-left corner of a super-pixel for a given size, which are referred to as the set $\hat{\mathbf{\Omega}}$. The set $\hat{\mathbf{\Omega}}$ is updated either by removing the point $(\hat{i}, \hat{j})$ as in line 18 when the super-pixel is not constructed, or by removing the set $\mathbf{B}$ as in line 16 when the super-pixel is constructed.

Notice that, before analyzing the MSE, the algorithm verifies whether the $2^{\eta} \times 2^{\eta}$ super-pixel can be constructed with the available pixels in $\mathbf{\Omega}$. Mathematically, the new super-pixel should satisfy $\mathbf{B} = \{(i,j) | (i,j) \in \mathbf{\Omega}\}$. Algorithm 2 repeats the operations in lines 6 to 20 until all points in $\hat{\mathbf{\Omega}}$ have been analyzed for super-pixels of size $2^{\eta} \times 2^{\eta}$, i.e. $|\hat{\mathbf{\Omega}}| = 0$. Then, the size is decreased as indicated in $\mathbf{S}$ by changing the index $z = z + 1$, and the procedure in lines 4 to 22 is performed until all pixels have been assigned to a super-pixel, i.e. $|\mathbf{\Omega}| = 0$. The size of the resulting matrix $\mathbf{\Delta}$ varies according to the data under analysis, however its number of rows is less than the original amount of unknowns to recover as shown in Eq. 16.

3.2 Design of Multi-resolution matrix ($\mathbf{\Delta}$) for irregular super-pixels

In applications where reconstruction speed is critical, irregular super-pixels can be used instead of the rectangular. The main goal is to group pixels with similar spectral normalized signatures into a super-pixel. The difference with the rectangular approach is that in this case, pixels from any location within the image can be grouped into a single super-pixel as indicated in Algorithm 3.

Thus, faster reconstructions can be attained because the amount of resulting super-pixels is less than that of the rectangular case. In other words, the irregular super-pixel approach

Algorithm 2 Algorithm to determine MR matrix $\mathbf{\Delta}$ for rectangular super-pixels

Input: FR fast reconstruction $\bar{\mathbf{F}}$, set of coordinate points $\mathbf{\Omega}$, tolerance σ, super-pixel size parameter η, data cube dimensions M, N
Output: MR decimation matrix $\mathbf{\Delta}$
Initialize super-pixel sizes $\mathbf{S} = [2^\eta, 2^{\eta-1}, \ldots, 1]$, $z = 0$, $c = 0$
while $|\mathbf{\Omega}| > 0$ **do**
    $\hat{\mathbf{\Omega}} = \mathbf{\Omega}$ Generate a new set of available points
    while $|\hat{\mathbf{\Omega}}| > 0$ **do**
        $(\hat{i}, \hat{j}) \in \hat{\mathbf{\Omega}}$ Choose a random point
        $\mathbf{B} = \{(i, j) | i = [\hat{i}, \hat{i}+1, \ldots, \hat{i} + \mathbf{S}(z)], j = [\hat{j}, \hat{j}+1, \ldots, \hat{j} + \mathbf{S}(z)]\}$ Generate the super-pixel $\mathbf{B}$ of size $\mathbf{S}(z)$ and a new top-left corner point $(\hat{i}, \hat{j}) \in \hat{\mathbf{\Omega}}$
        $\mathbf{p} = E\{\bar{\mathbf{F}}_\mathbf{B}\}$ Calculate the average spectrum in $\mathbf{B}$
        if $max(MSE(\mathbf{p}, \bar{\mathbf{F}}_\mathbf{B})) < \sigma$ **then**
            $\mathbf{\Gamma} = \mathbf{0}_{M \times N}$
            $\mathbf{\Gamma}_{(i,j)} = 1$ for $(i, j) \in \mathbf{B}$ Create indicator matrix
            $(\mathbf{\Delta})_c = vec(\mathbf{\Gamma})$ Vector form of $\mathbf{\Gamma}$ is assigned as a new row of MR matrix
            $c = c + 1$ Update MR super-pixels counter
            $\mathbf{\Omega} = \mathbf{\Omega} - \mathbf{B}$ Update available points
            $\hat{\mathbf{\Omega}} = \hat{\mathbf{\Omega}} - \mathbf{B}$ Update eligible points for analysis
        else
            $\hat{\mathbf{\Omega}} = \hat{\mathbf{\Omega}} - (\hat{i}, \hat{j})$ Remove the corner point from the set of eligible points
        end if
    end while
    $z = z + 1$ Change super-pixel size index
end while

can be seen as a fast clustering approach, where each cluster is a super-pixel.

The inputs for the algorithm are the set of spatial coordinates of the image $\mathbf{\Omega}$, the interpolated scene $\bar{\mathbf{F}}$ and the error tolerance σ, in this kind of super-pixels the parameter for the super-pixel size is not necessary since it is determined by the spectral similarity of the pixels in the image and the threshold σ.

The main idea in this approach is to compare the spectral signature of a spatial point with respect to all other points in the image such that those with similar spectral responses, according to the threshold σ, are grouped into a super-pixel. For this purpose, algorithm 3 randomly chooses a spatial point $(\hat{i}, \hat{j})$ from $\mathbf{\Omega}$, and calculates the MSE between the normalized signature of this point $\mathbf{p} = \bar{\mathbf{F}}_{(\hat{i},\hat{j})}$ and all other points (i, j) in $\mathbf{\Omega}$. The super-pixel is then defined by those points satisfying $\mathbf{B} = \{(i, j) \in \mathbf{\Omega} | (MSE(\mathbf{p}, \bar{\mathbf{F}}_{(i,j)}) < \sigma\}$ as in line 7 from Algorithm 3. As in the rectangular case, an indicator matrix represents the pixels assigned to $\mathbf{B}$, and is defined as

$$\mathbf{\Gamma}_{(i,j)} = \begin{cases} 1 & for \quad (i,j) \in \mathbf{B} \\ 0 & otherwise \end{cases}, \tag{19}$$

Then, the vectorized form of $\mathbf{\Gamma}_{(i,j)}$ is added as a new row of Δ, as shown in line 9 of Algorithm 3. To guarantee that each pixel is assigned to only one super-pixel, the set of pixels in $\mathbf{B}$ is removed from $\mathbf{\Omega}$ as $\mathbf{\Omega} = \mathbf{\Omega} - \mathbf{B}$. The process is then repeated until all pixels have been assigned to a super-pixel. i.e. $|\mathbf{\Omega}| = 0$.

Algorithm 3 Algorithm to determine MR decimation matrix $\mathbf{\Delta}$ for irregular super-pixels

1: **Input:** FR fast reconstruction $\bar{\mathbf{F}}$, set of coordinate points $\mathbf{\Omega}$, tolerance σ
2: **Output:** MR decimation matrix $\mathbf{\Delta}$
3: $c = 0$ Initialize super-pixel count
4: **while** $|\mathbf{\Omega}| > 0$ **do**
5: $\quad (\hat{i}, \hat{j}) \in \mathbf{\Omega}$ Select a point
6: $\quad \mathbf{p} = \bar{\mathbf{F}}_{(\hat{i},\hat{j})}$ Extract spectral signature
7: $\quad \mathbf{B} = \{(i, j) \in \mathbf{\Omega} | (MSE(\mathbf{p}, \bar{\mathbf{F}}_{(i,j)}) < \sigma\}$ Select set of points with similar spectrum to $\mathbf{p}$
8: $\quad \mathbf{\Gamma}_{(i,j)} = 1$ for $(i, j) \in \mathbf{B}$
9: $\quad (\mathbf{\Delta})_c = vec(\mathbf{\Gamma})$ Vector form of $\mathbf{\Gamma}$ is assigned as a new row of MR matrix
10: $\quad \mathbf{\Omega} = \mathbf{\Omega} - \mathbf{B}$ Delete selected points from the set
11: $\quad c = c + 1$ Update the super-pixel index
12: **end while**

3.3 Design of Multi-resolution decimation matrix ($\boldsymbol{\Delta}$) using Simple Linear Iterative Clustering (SLIC) super-pixels

The SLIC algorithm is an approach developed for design the super-pixels for compression in post-processing of RGB images[32], for build the super-pixel on the SLIC algorithm, first define centers $C_i = [l_{1_i}, l_{2_i}, l_{3_i}, x_i, y_i]^T$, where l_{1_i}, l_{2_i}, l_{3_i} are the values in each spectral band of the RGB image, and x_i, y_i the spatial location, these centers are sampled on a regular grid spaced $S = \sqrt{N/n}$, where n is the number of desired super-pixels. Next, the centers are moved to seed locations corresponding to the lowest gradient position in a 3×3 neighborhood, later, for each point in a $2S \times 2S$ region around each C_i the distance $\bar{d}$ is calculated, and if $\bar{d}$ to the center C_i is the lowest then this pixel is assigned to the super-pixel that correspond to the center C_i, where the distance is calculated as

$$\begin{aligned} \bar{d} &= \sqrt{d_c^2 + \left(\frac{d_s}{S}\right)^2 p^2} \\ d_c &= \sqrt{(l_1 - l_1')^2 + (l_2 - l_2')^2 + (l_3 - l_3')^2} \\ d_s &= \sqrt{(x - x')^2 + (y - y')^2} \end{aligned} \tag{20}$$

where p allows us to weigh the relative importance between color similarity and spatial proximity

In this work the SLIC super-pixel method is employed because of its low complexity $\Theta(N)$, and high segmentation accuracy, it is important to note that SLIC super-pixels have been designed for being used in RGB images i.e. 3-band images, and if the number of bands is greater than 3, the measure of the distance should be modified and this modification augments the computational load. For this reason, we first calculate an equivalent 3-band version of the SI $\bar{\mathbf{F}}$, which can be obtained as

$$\tilde{\mathbf{F}}_{(i,j,r)} = \frac{1}{\delta_L} \sum_{l=1+(r-1)\delta_L}^{r\delta_L} \bar{\mathbf{F}}_{(i,j,l)}, \tag{21}$$

where $\delta_L = round(L/3)$ and $r = 1, 2, 3$, this step is illustrated in fig. 7.

Then, using the SLIC approach the super-pixels in this three-band version of the scene $\tilde{\mathbf{F}}$ are determined. SLIC algorithm requires an input parameter υ, which indicates the number of equally-sized super-pixels of the resulting image. This parameter is used to determine the approximate size of the super-pixels as $S = \sqrt{NM/\upsilon}$. The main idea of the SLIC algorithm is to use the similarities of the pixels in a neighborhood of $2S \times 2S$ around of a center pixel,

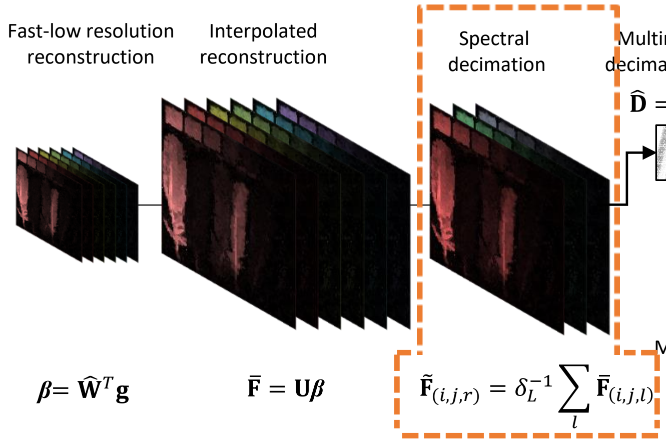

Figure 7: Proposed multi-resolution (MR) reconstruction process using SLIC super-pixels, notice that $\boldsymbol{\xi}$ is calculated solving the minimization problem in Eq. 16.

but the actual super-pixel size is only $S \times S$. The center pixel is updated for each super-pixel until all pixels in the image have been assigned. This algorithm is described with more detail in [31]. Fig. 8 illustrates the super-pixel map for different number of super-pixels υ, which show that for a lower value of υ the super-pixels built are bigger than for a higher value of υ, but in both cases, the super-pixels have a good distribution in the spectral image keeping the edges.

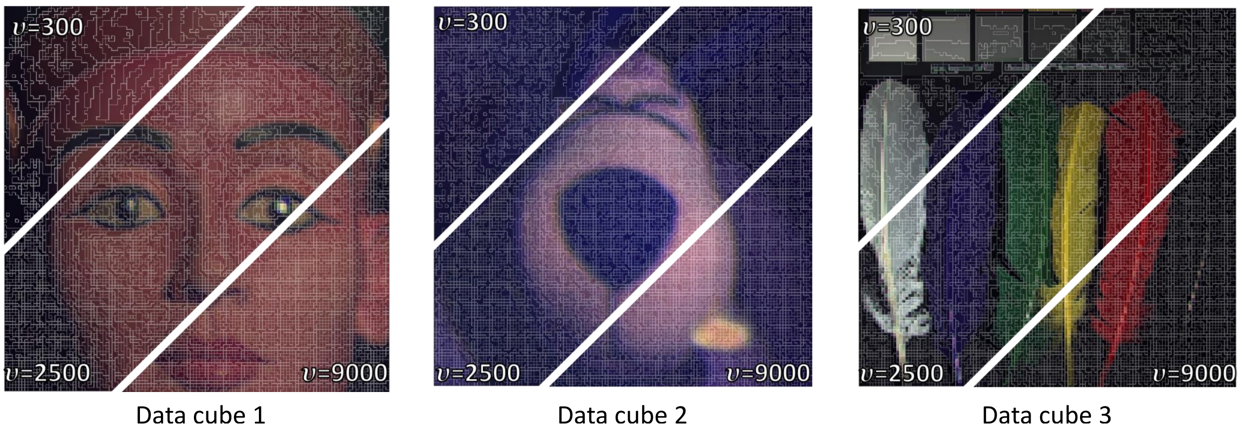

Figure 8: Visual comparison of the super-pixels map, using three different number of super-pixels υ for the three test data cubes with original spatial resolution 128 × 128 pixels

The super-pixel map is binarized in $\boldsymbol{\Upsilon}_s$, where s is the super-pixel index, such that the pixels belonging to the same super-pixel take value one and the others zero, for each generated super-pixel. Each binarized super-pixel map is vectorized and added as a new row of the decimation matrix $\boldsymbol{\Delta}$, whose total number of rows is υ . An example of this process is illustrated in Fig. 9

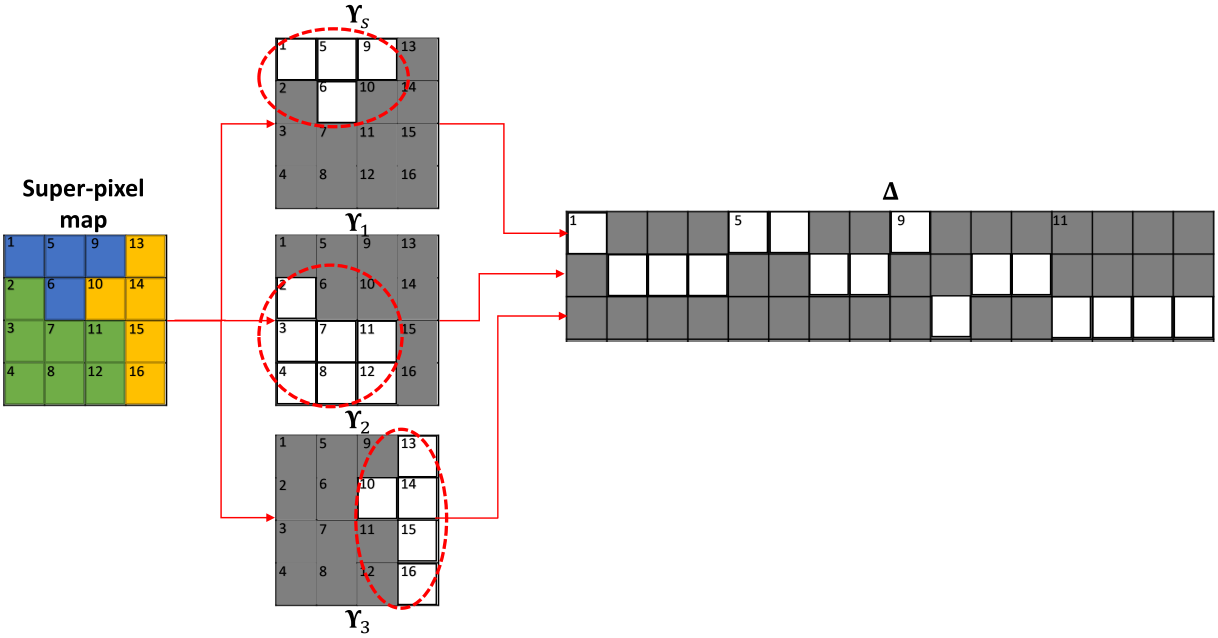

Figure 9: Example of the decimation matrix ($\mathbf{\Delta}$) generation. White squares represent 1, and gray zones are 0. Three super-pixels are obtained from the 4×4 image.

3.4 Computational Complexity

As it was previously mentioned, the problem in Eq. 16 has computational complexity $O(KCL)$, where K and L do not depend on the method to design the MR decimation matrix. Contrarily, the number of super-pixels, C, is indeed directly related with the method employed to generate the MR matrix. Specifically, when rectangular super-pixels are used, and the MR matrix $\mathbf{\Delta}$ is generated as in Algorithm 2, the resulting number of super-pixels, C, depends on the parameter η, which determines the super-pixels sizes. Moreover, C also depends on the error tolerance threshold (σ), which determines the spectral similarity between pixels. Note that in general, C also depends on the characteristics of the scene to reconstruct. Specifically, Smooth scenes will result in a smaller number of possibly large super-pixels, while more detailed scenes yield a larger value for C, i.e. smaller super-pixels.

On the other hand, when the MR matrix is generated using the irregular super-pixel approach summarized in Algorithm 3, the value of C depends on the threshold σ, which determines the spectral similarity between pixels and the scene to reconstruct, because in this method all super-pixel sizes are allowed. Finally, the SLIC-based MR decimation matrix requires the amount of desired super-pixels (υ) as an input parameter. Therefore, in this case the computational complexity of solving the problem in Eq. 16 only depends on υ, which is close to C, i.e. $C \approx \upsilon$. Table 1 summarizes the parameters that determine the computational complexity for each discussed case.

Table 1: Summary of the parameters that determine the computational complexity for each MR decimation approach

Method	**Parametric dependence of C**
Rectangular super-pixels	Scene to reconstruct, σ and η
Irregular super-pixels	Scene to reconstruct and σ
SLIC	Amount of desired super-pixels υ

Chapter 4

Simulations and results

Several simulations were realized to test the performance of the proposed methods. Two different data cubes $\mathbf{F}$ with 128×128 pixels of spatial resolution were used, changing the number of bands L from 3 to 30. Two data cubes are test spectral images from [33]. For each data base, SPC compressive measurements are obtained as in Eq. 9 with a compression ratio $\gamma = 0.25$. The proposed MR reconstruction scheme using SLIC, rectangular and irregular super-pixels was employed with the simulated measurements, and reconstructions were obtained using the gradient projection for sparse reconstruction (GPSR) algorithm [34], which solves the inverse problem from Eq. 16. Attained reconstructions are compared with respect to the traditional full-resolution reconstruction approach in Eq. 1, using the same number of iterations for both cases. The comparisons are expressed in terms of peak signal to noise ratio (PSNR), structural similarity (SSIM), and complexity/time of reconstructions (seconds). The regularization parameter for the GPSR algorithm was selected such that each simulation uses the value that results in the best reconstruction. A $3D$ representation basis $\mathbf{\Psi} = \mathbf{\Psi}_C \otimes \mathbf{\Psi}_{2D}$ was used, where $\mathbf{\Psi}_C$ is the $1D$ discrete cosine transform and $\mathbf{\Psi}_{2D}$ is a $2D$ Wavelet Symmlet 8 basis. It is worth noting that the number of super-pixels for both approaches is a dyadic value, such that the wavelet representation of the signal can be computed. All simulations were conducted and timed using an Intel Core i7-6700 @3.40GHz processor, and 32 GB RAM memory.

4.1 Fast low resolution reconstructions

To illustrate the results of the LR approximations used as starting point of the proposed scheme, this experiment presents the fast LR reconstructions $\boldsymbol{\beta}$ obtained with Eq. 12, each with a spatial resolution of 64×64. Figure 10 shows RGB versions of the LR reconstructions compared with the corresponding decimated versions of the ground truth for $L = 6$. To illustrate the spectral similarity between both LR images, Figs. 11 and 12 shows the spectral bands for the first data cube. In addition, the spectral responses of two points of each scene are shown in Fig. 13. Notice that the normalized spectral response in all cases is close to that of the ground truth.

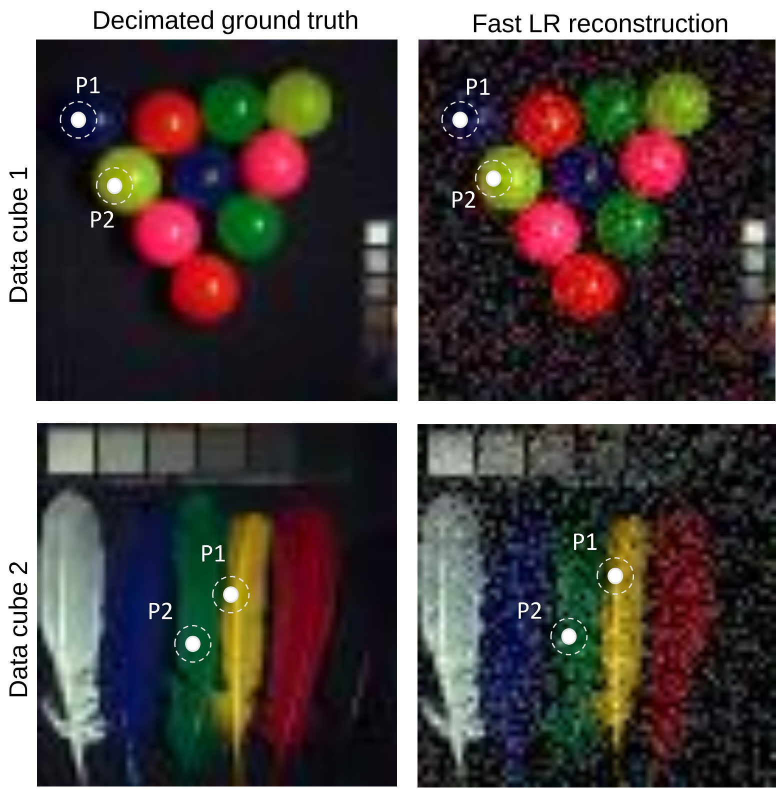

Figure 10: RGB version of the low resolution versions of the two data cubes with 64×64 pixels

4.2 Map of super-pixels

The interpolated versions of the results from the previous section, calculated using Eq. 14, were used as an input to build the super-pixels based on rectangular, irregular and SLIC

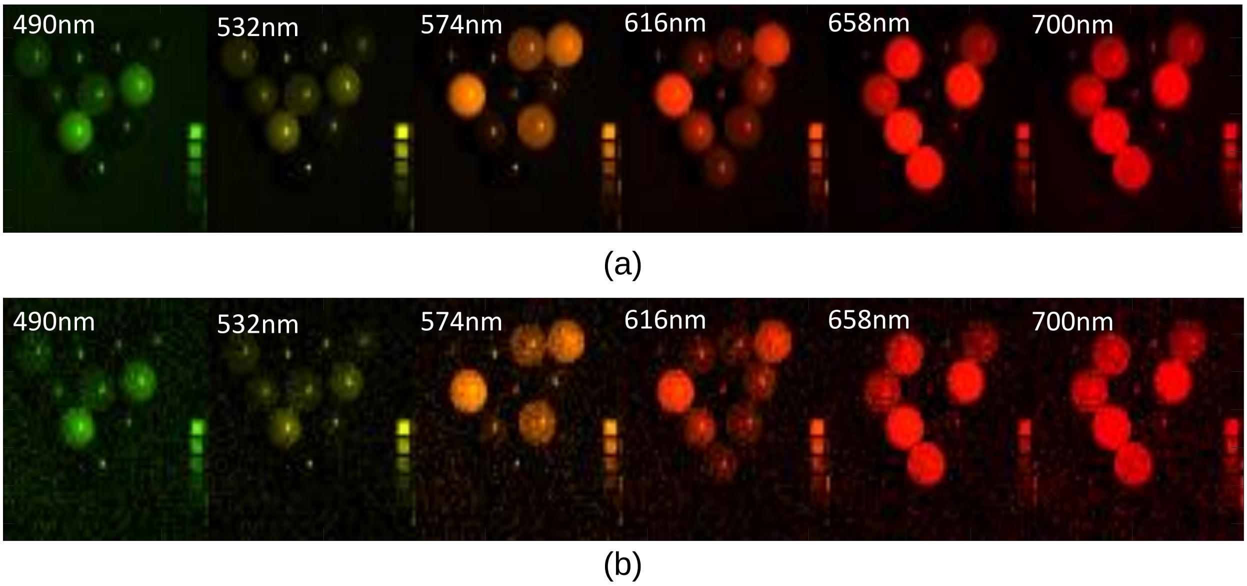

Figure 11: Six spectral bands from data cube 1, each spectral slice has a spatial resolution of 64×64 pixels, (a)Decimated ground truth. (b) Fast LR reconstruction

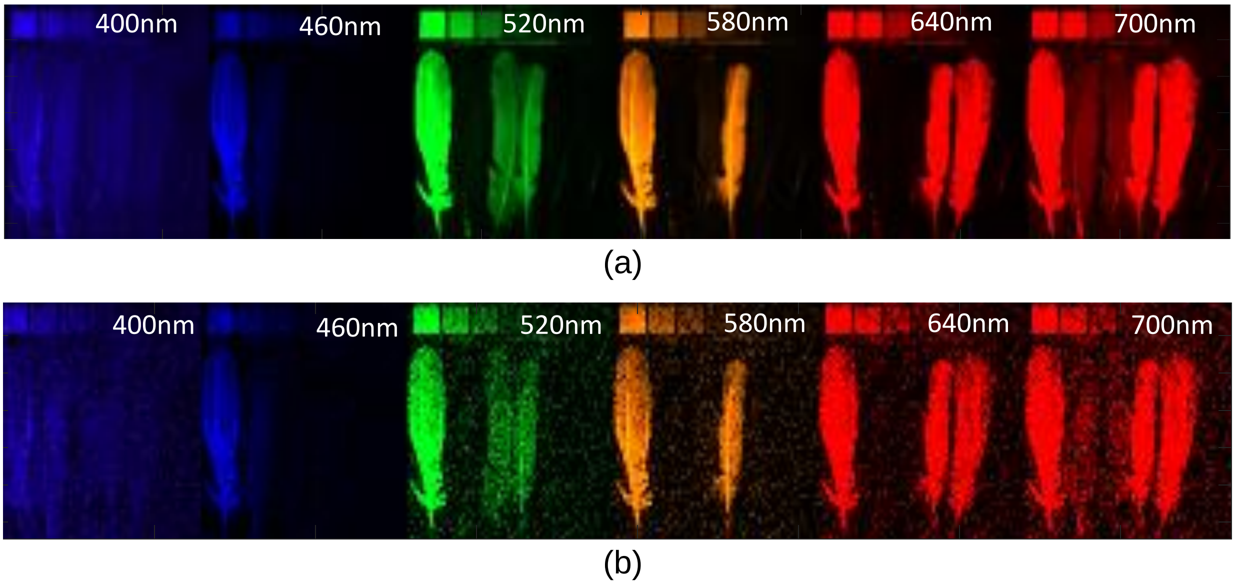

Figure 12: Six spectral bands from data cube 2, each spectral slice has a spatial resolution of 64×64 pixels, (a)Decimated ground truth. (b) Fast LR reconstruction

approaches, in order to generate the maps of super-pixels that are associated to the MR decimation matrix Δ, for each case. Figure 14 illustrates the obtained super-pixel maps for each case and the two data cubes. Each color represents a different super-pixel size denoted as η, and the grid illustrates the super-pixel map for the rectangular cases. Notice that in zones with more spectral variations the super-pixels are smaller than those from smooth

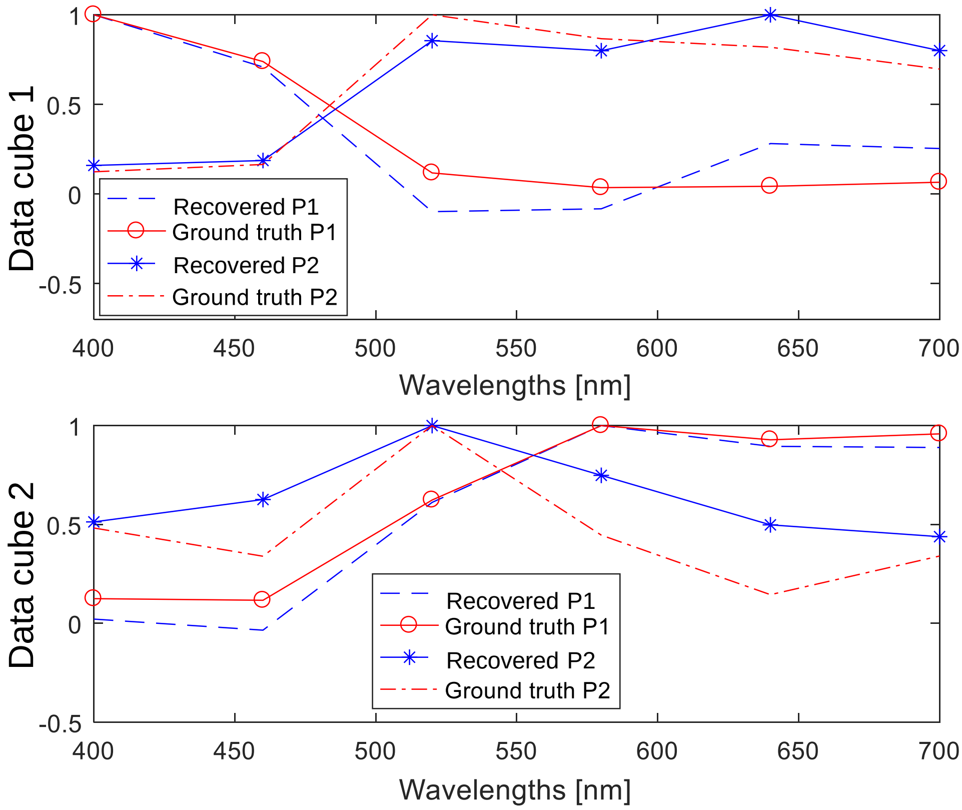

Figure 13: Spectral signatures of the highlighted points in Fig. 10

zones. The largest rectangular super-pixel designed for these scenes was 4×4. On the other hand, for the irregular case, each color represents a single super-pixel. In other words, pixels belonging to the same super-pixel are shown with the same color. And for the SLIC super-pixels the grid indicates the super-pixel map.

4.3 Multi-resolution reconstructions

The MR reconstructions for the two data cubes were obtained using the decimation matrices Δ associated to the maps of super-pixels from Chapter 4 and Eq. 17. Figure 15 shows the average reconstruction PSNR, SSIM, and the computation time for the two data cubes using the traditional full-resolution reconstruction from Eq. 1, and the MR reconstruction with rectangular, irregular and SLIC super-pixels. The results are presented as a function of the recovered number of spectral bands L.

These figures show that the proposed MR reconstruction approach improves the traditional full-resolution reconstruction. Specifically, for the first data cube (Color balls), the irregular super-pixels provide the best reconstruction with up to $6dB$ of PSNR and 0.38 in

SSIM improvements over the traditional approach. However, for the second data cube, the best results are obtained with the SLIC super-pixel MR reconstruction, with improvements of up to $6dB$ of PSNR and 0.3 SSIM over the traditional approach. In addition, in relation to the computation time required for each approach, it can be noticed that the MR reconstructions with irregular, rectangular and SLIC super-pixels are up to 96%, 82%, 93% faster than the full-resolution reconstructions for the first data cube, and up to 93%, 59%, 93% faster for the second data cube, respectively.

Furthermore, Figs. 16 and 18 illustrate an RGB mapping of the attained reconstructions for the two data cubes, respectively. Specifically, the MR reconstructions with rectangular, irregular and SLIC super-pixels are compared with the traditional full-resolution reconstruction from Eq. 1, and also with the ground truth. In addition, Fig. 17 and 19 presents a comparison of the recovered spectral bands for both data cubes, where the improvements of the irregular and SLIC super-pixels approaches are clearly noticeable for the first data cube and the second data cube, respectively.

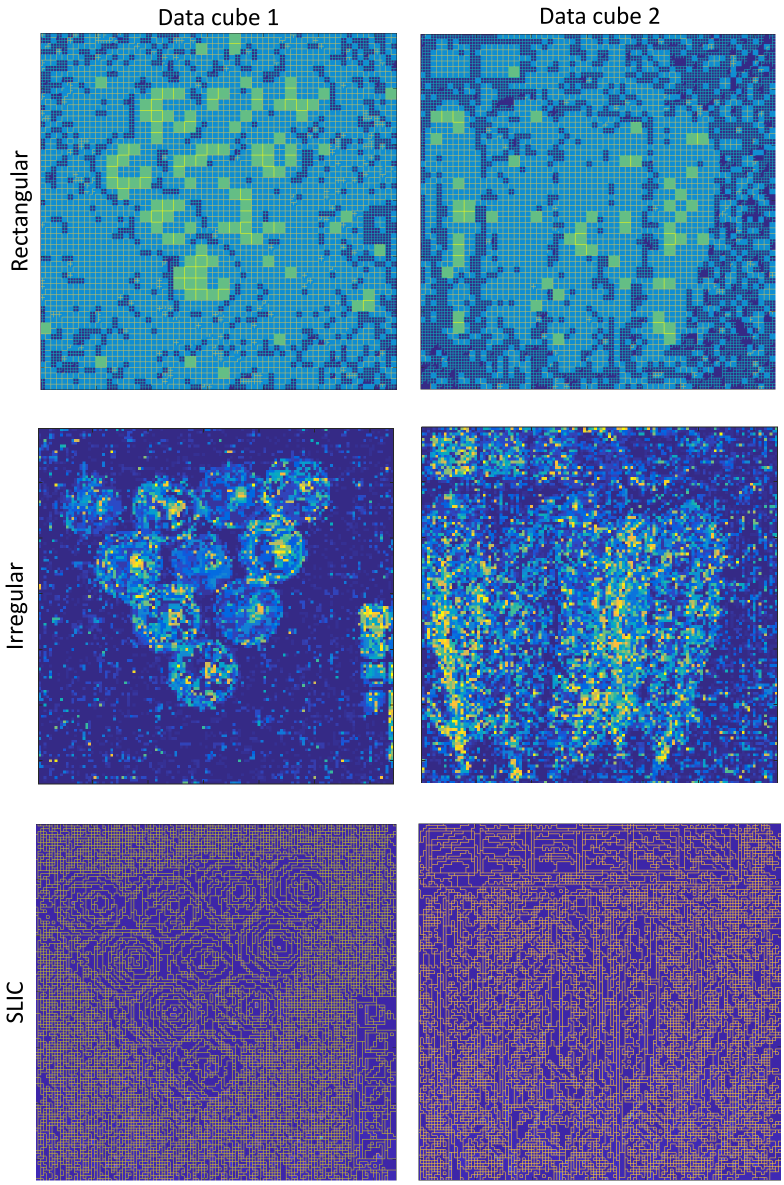

Figure 14: Map of super-pixels for rectangular,irregular and SLIC approaches for two data cubes.

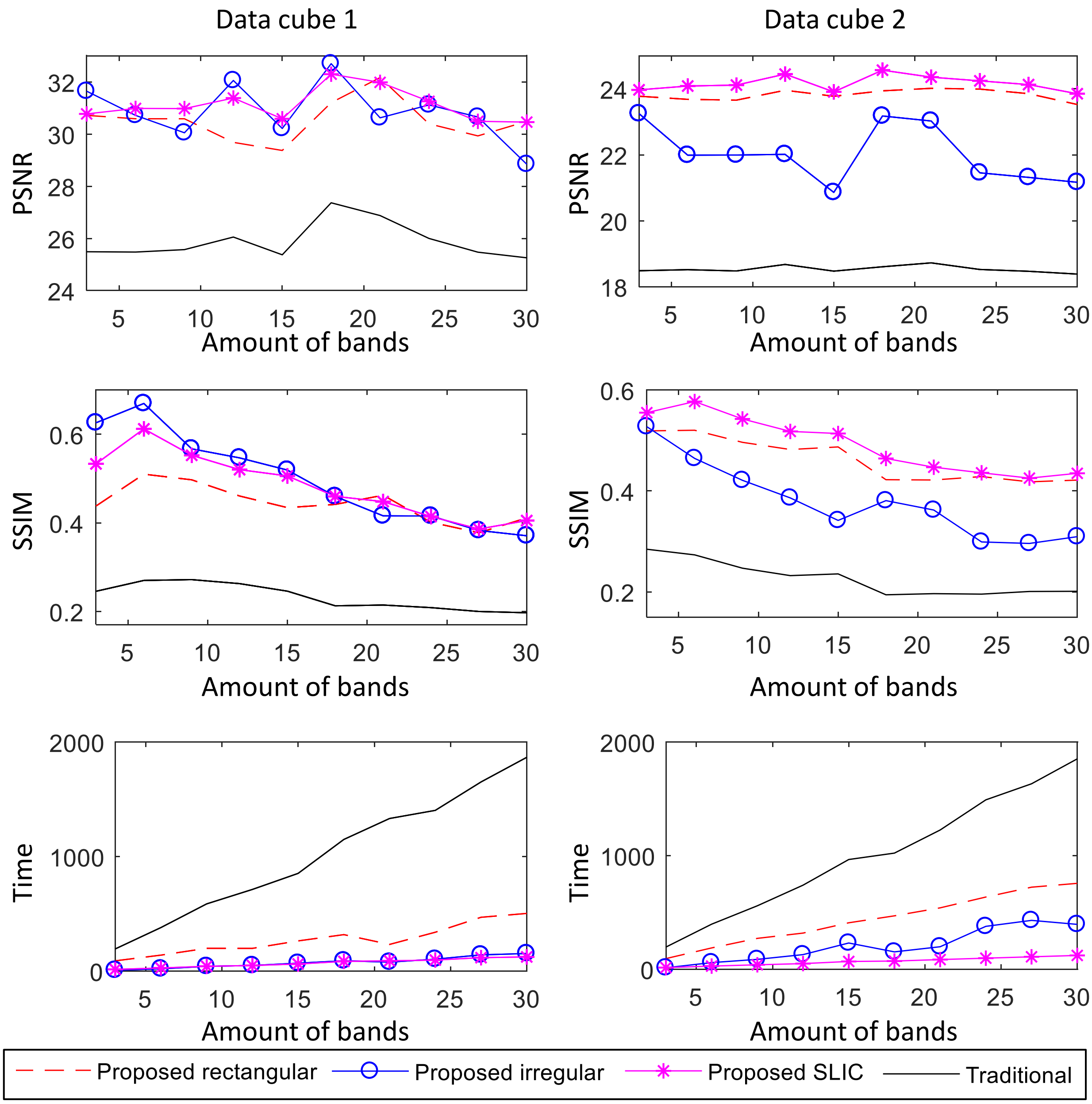

Figure 15: Comparison of the MR and traditional approaches in terms of the PSNR, SSIM and computation time for the two data cube varying the number of spectral bands, with spatial resolution 128×128.

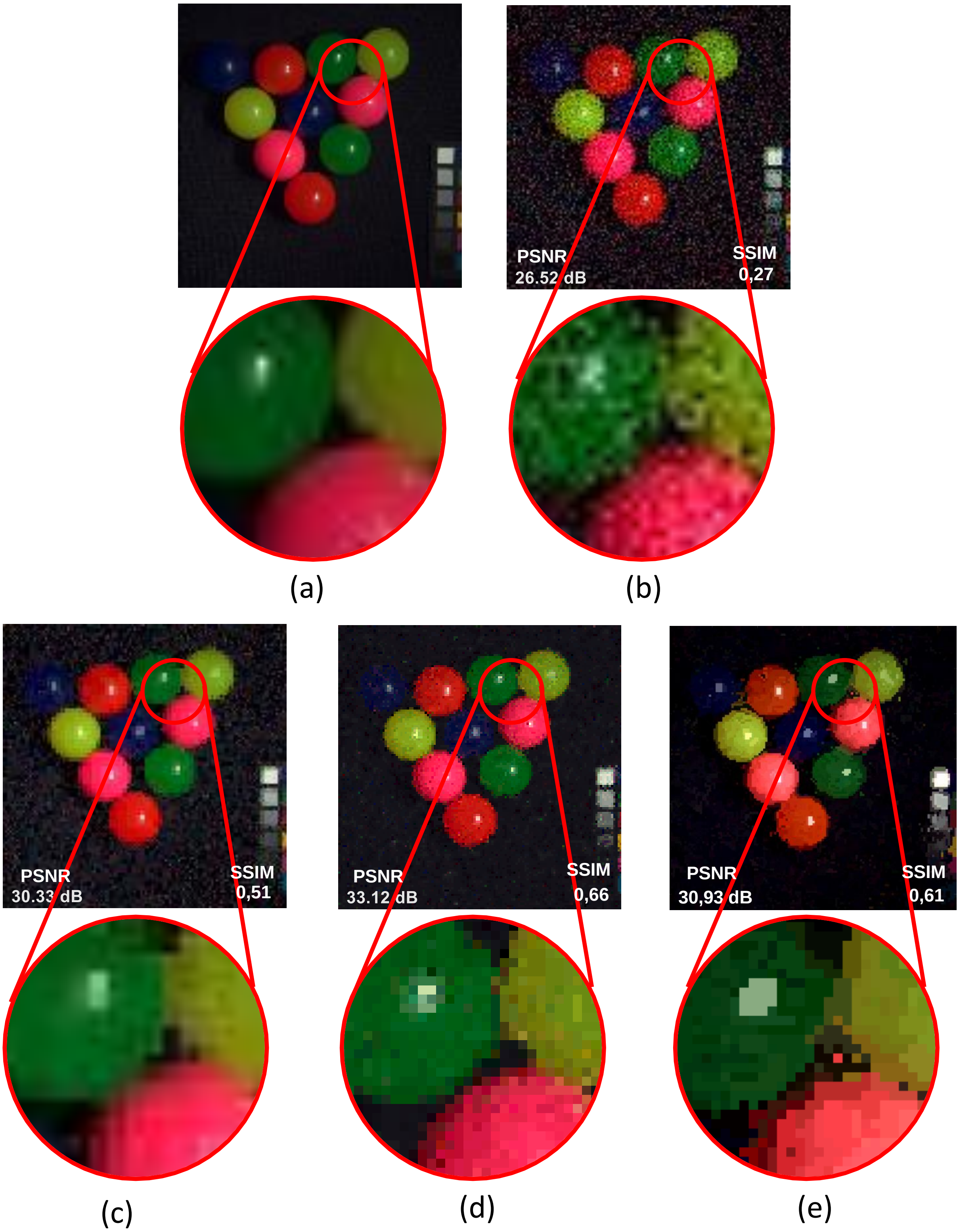

Figure 16: RGB Comparison between the ground truth with the different reconstruction approaches for data cube 1 with spatial dimensions 128×128 and $L = 6$. (a)ground truth; (b)reconstruction using traditional approach; and multi-resolution reconstruction using (c) rectangular super-pixels, (d) irregular super-pixels and (e) SLIC super-pixels.

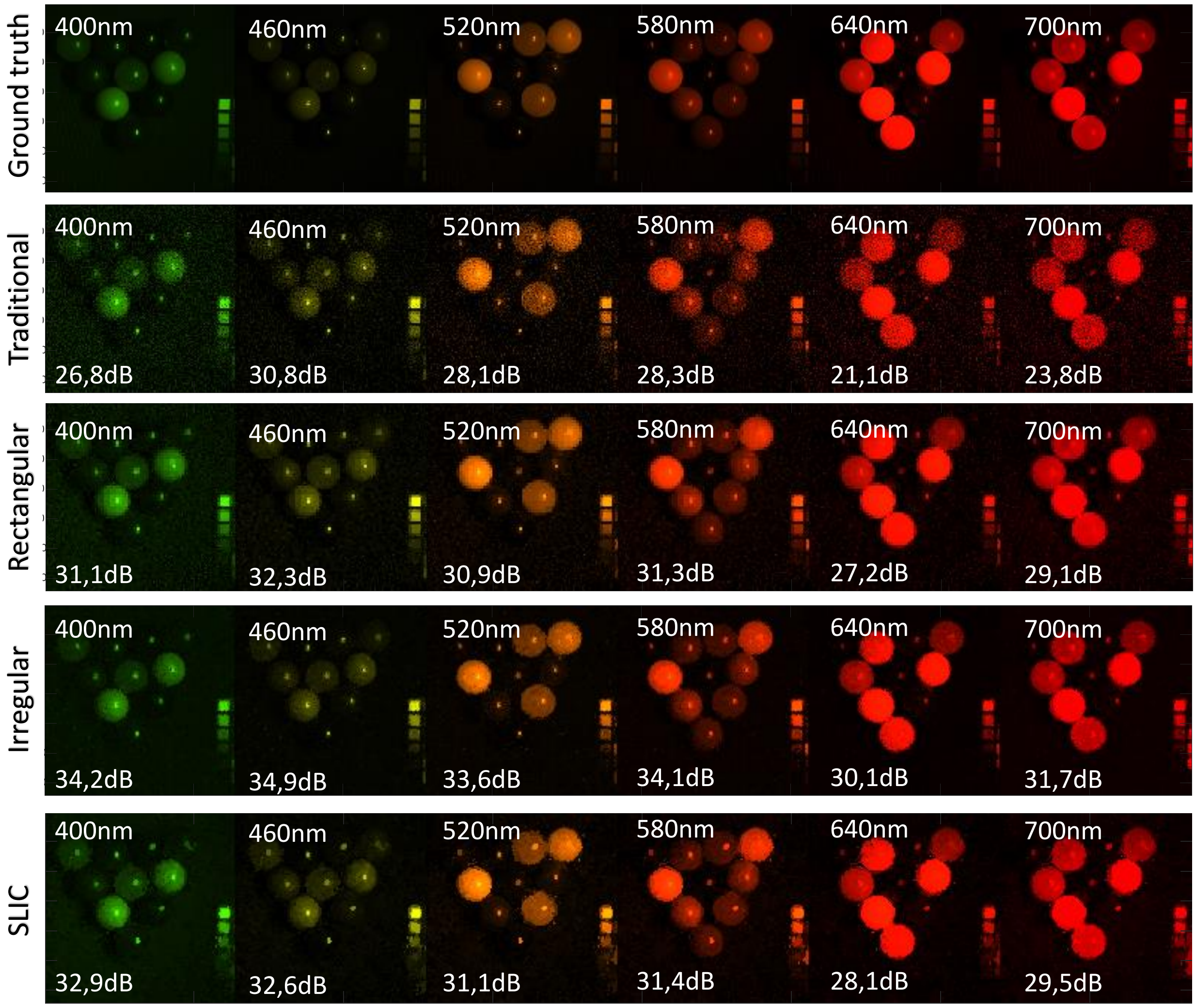

Figure 17: Comparison of spectral bands between the ground truth with the different reconstruction approaches for data cube 1, with $M = N = 128$, $L = 6$.

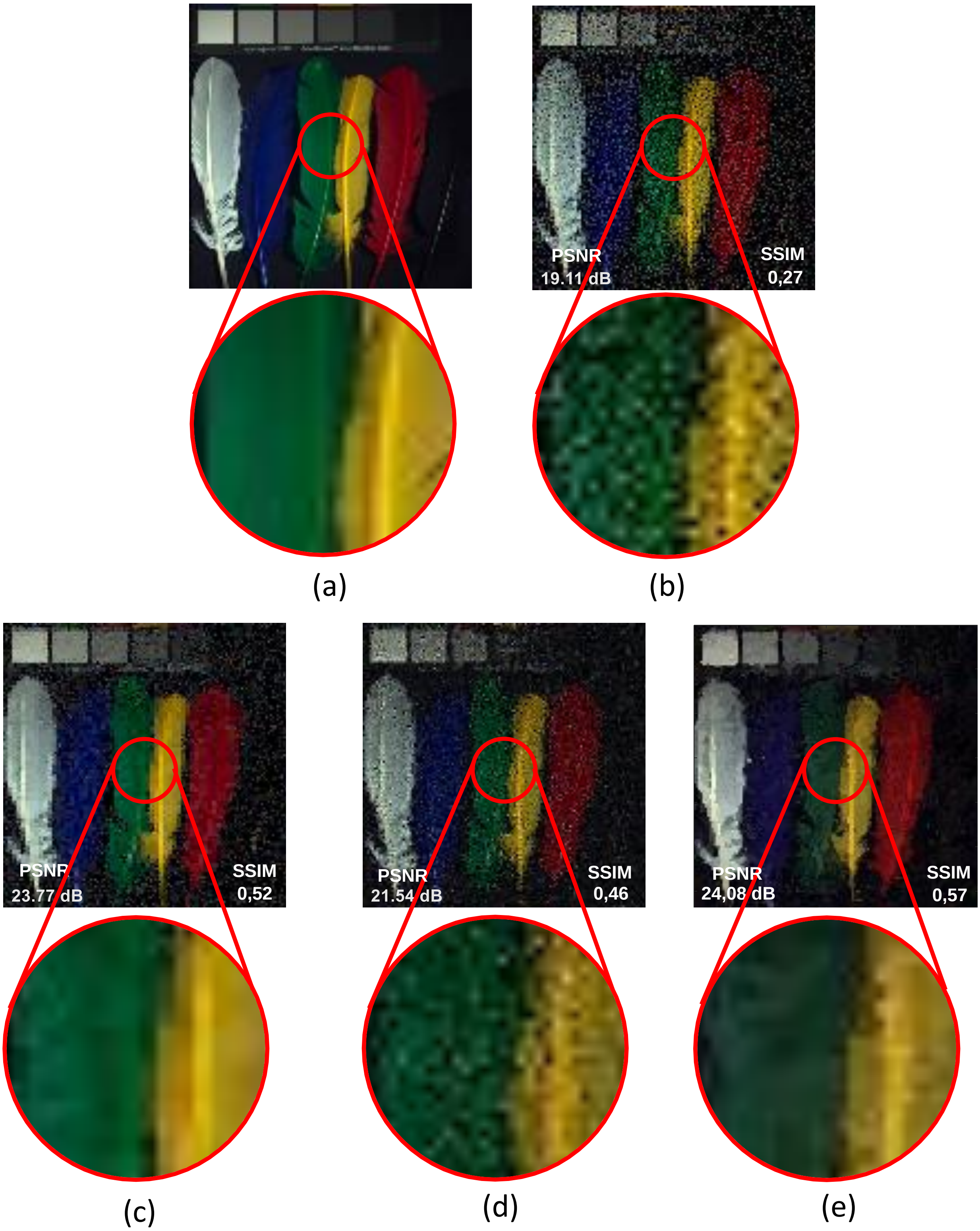

Figure 18: RGB Comparison between the ground truth with the different reconstruction approaches for data cube 2 with spatial dimensions 128×128 and $L = 6$. (a)ground truth; (b)reconstruction using traditional approach; and multi-resolution reconstruction using (c) rectangular super-pixels, (d) irregular super-pixels and (e) SLIC super-pixels.

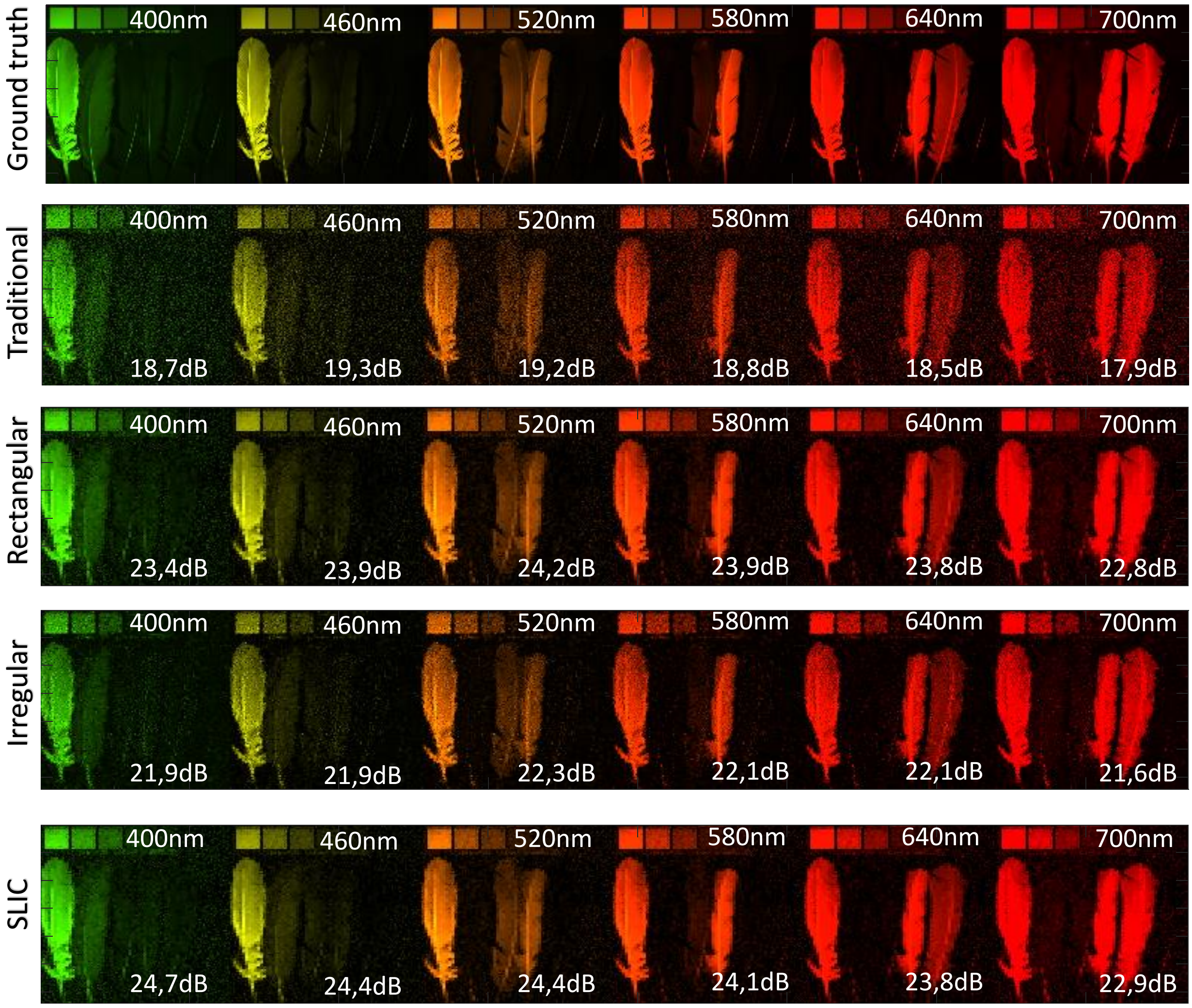

Figure 19: Comparison of spectral bands between the ground truth with the different reconstruction approaches for data cube 2, with $M = N = 128$, $L = 6$.

Chapter 5

Experimental setup and results

An optical test bed implementation of the SPC was constructed in the laboratory to experimentally verify the proposed reconstruction methodology. This prototype is shown in Fig. 20, and is composed by a $50mm$ objective lens; a digital micromirror device (DMD) as encoding element; a $100mm$ relay lens; and a F220SMA-A condenser connected through a fiber with an Ocean Optics Flame S-VIS-NIR-ES spectrometer used as detector. Specifically, the DMD is placed at the image plane of the imaging lens. For this reason, the selection of the objective lens depends on the desired image resolution, which is determined by the active area of the DMD. In this way, a focused image is obtained at the DMD and, a correct spatial coding is performed as described in Chapter 4.

Afterwards, a relay lens directs the encoded rays, reflected by the DMD, to the condenser lens, which draws them to a single point where the optical fiber transmits them to the spectrometer. To guarantee that the whole scene is concentrated within the field of view of the condenser lens, it is placed at the image plane of the relay lens.

It is important to remark that the Flame spectrometer provides 2048 equispaced spectral bands of the concentrated coded scene, in the range from $339nm$ to $1023nm$. In this work this range was reduced to $400nm$ to $750nm$, because a good signal to noise ratio is attained when using the lamp for the visible spectrum available at the HDSP electronic optical lab. In this range, the spectrometer measure 1000 bands. The desired number of spectral bands is obtained by averaging the acquired visible spectrum in similar width bins. For instance, to obtain $L = 200$ bands, the spectral range is divided into sets of 5 bins, and each resulting spectral band is the average of the bins on each set.

To acquire SPC measurements, the integration time of the Flame spectrometer was selected such that it uses the total dynamic range without saturating the sensor. The process to select this parameter consists on illuminating a white target, because it is the brightest possible scene, and select the higher integration time value for which the sensor is not saturated (65536 counts). With this configuration, the compressive measurements are acquired using a Matlab script that controls the synchronization between the coded aperture pattern refresh rates and the integration time of the spectrometer, such that each measurement is captured for the correspondent coded aperture pattern.

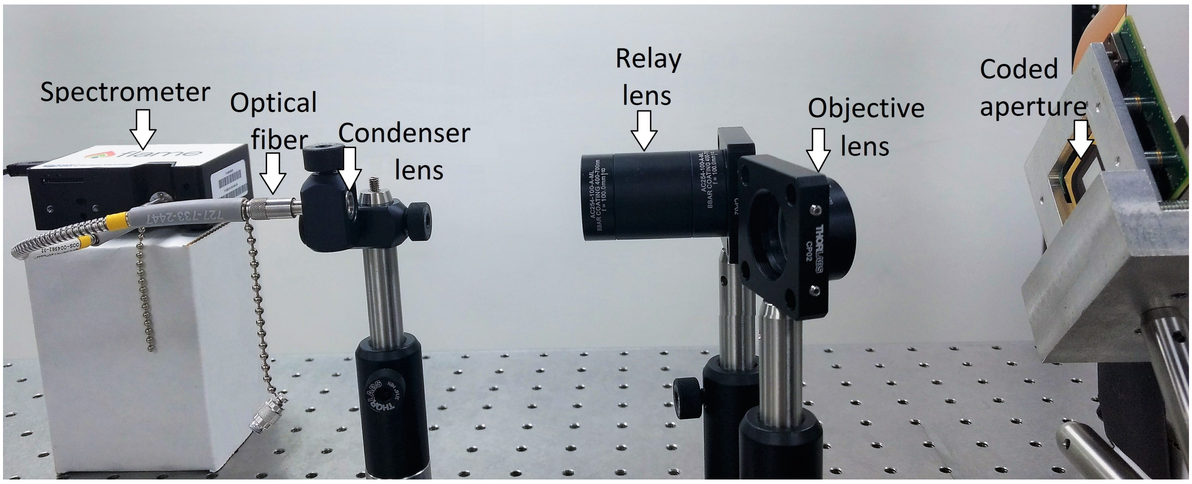

Figure 20: Test bed implementation of the SPC architecture.

It is important to remark that because the designed coded aperture is composed of 1 and -1 entries, and the DMD only can represent 1 and 0, the coded aperture is implemented as shown in Eq. 22. Specifically, an additional snapshot is captured using an all-ones coded aperture pattern. Notice that this shot does not affect the compression ratio. Denote $\bar{\mathbf{T}}^k$ as the coded aperture implemented by the DMD with entries 0 or 1. Similarly, denote an all-ones coded aperture pattern as $\mathbf{1}$. Then, the resulting coded aperture with entries -1 or 1 is given by

$$\mathbf{T}^k = 2\bar{\mathbf{T}}^k - \mathbf{1} \tag{22}$$

Using Eq. 22, the measurements from Eq. 6 are rewritten as

$$\begin{aligned} g_l^k &= \sum_i \sum_j \mathbf{F}_{(i,j,l)} \mathbf{T}^k_{(i,j)} = \sum_i \sum_j \mathbf{F}_{(i,j,l)} \left(2\bar{\mathbf{T}}^k_{(i,j)} - \mathbf{1}_{(i,j)}\right) \\ g_l^k &= 2\sum_i \sum_j \mathbf{F}_{(i,j,l)} \bar{\mathbf{T}}^k_{(i,j)} - \sum_i \sum_j \mathbf{F}_{(i,j,l)} \end{aligned} \tag{23}$$

Measurements of two different target scenes were captured with this system with a compression ratio $\gamma = 0.25$. Figures 21 and 22 show the RGB mappings of two reconstructed spectral scenes with 128×128 pixels of spatial resolution and $L = 30, 90, 200$, using the traditional full resolution reconstruction and the proposed MR reconstructions for rectangular, irregular and SLIC super-pixels. These results verify the simulation results and demonstrate that the proposed approach overcomes the traditional reconstruction from real measurements.

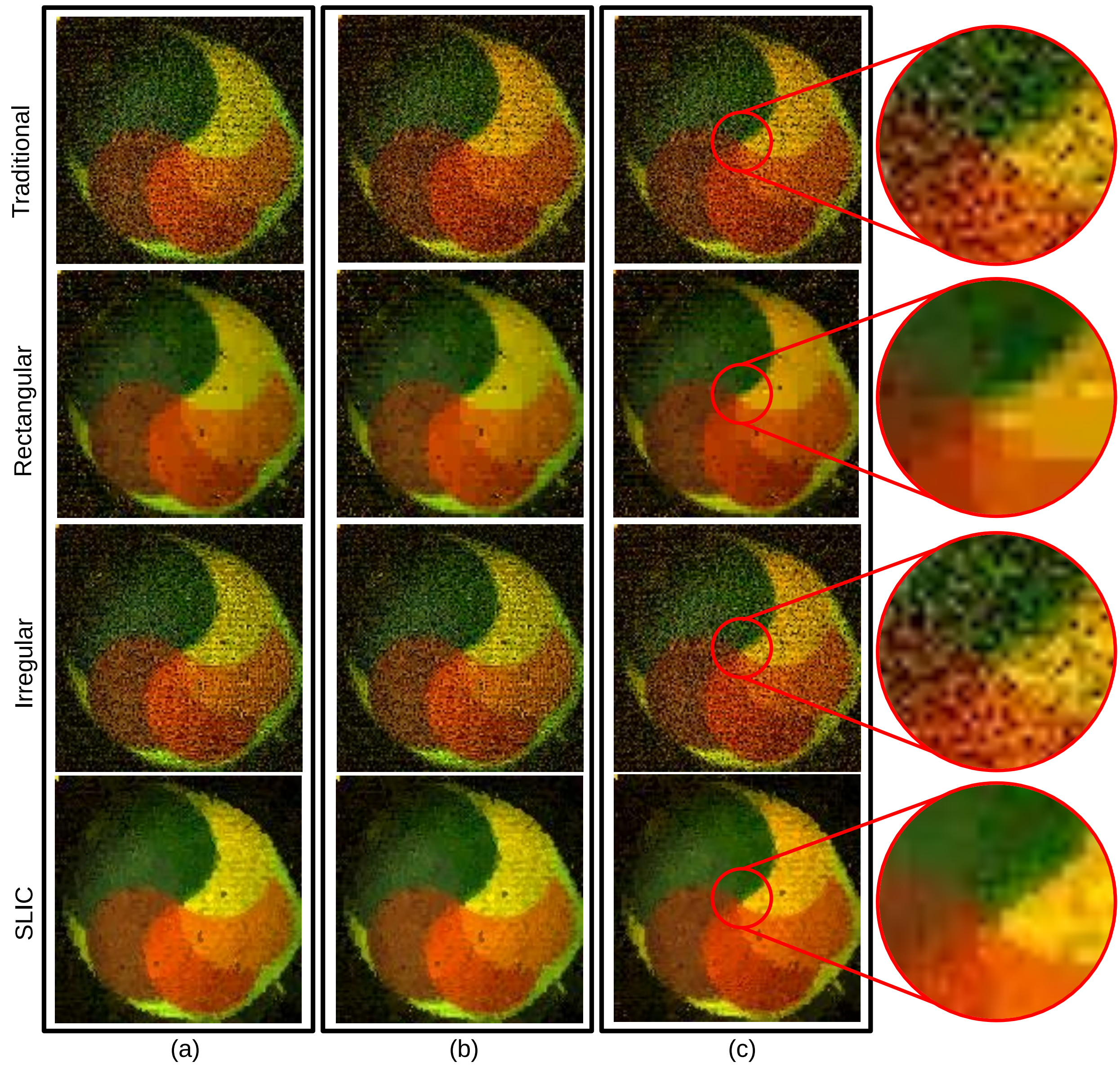

Figure 21: RGB comparison of the reconstructions, using the traditional approach and the proposed MR reconstruction with rectangular, irregular and SLIC super-pixels for $N = 128$, $M = 128$ and (a)$L = 30$ (b) $L = 90$ and (c)$L = 200$.

Furthermore, to verify the accuracy of the experimental results, the spectral signature of the recovered scenes is compared with the spectral signatures of the ground truth acquired directly with the spectrometer at two selected points P_1 and P_2 highlighted in Fig. 23. It can be seen that the proposed methods provide more accurate spectral approximations. In addition, Figs. 24 and 25 present a comparison of the recovered spectral bands for both real scenes.

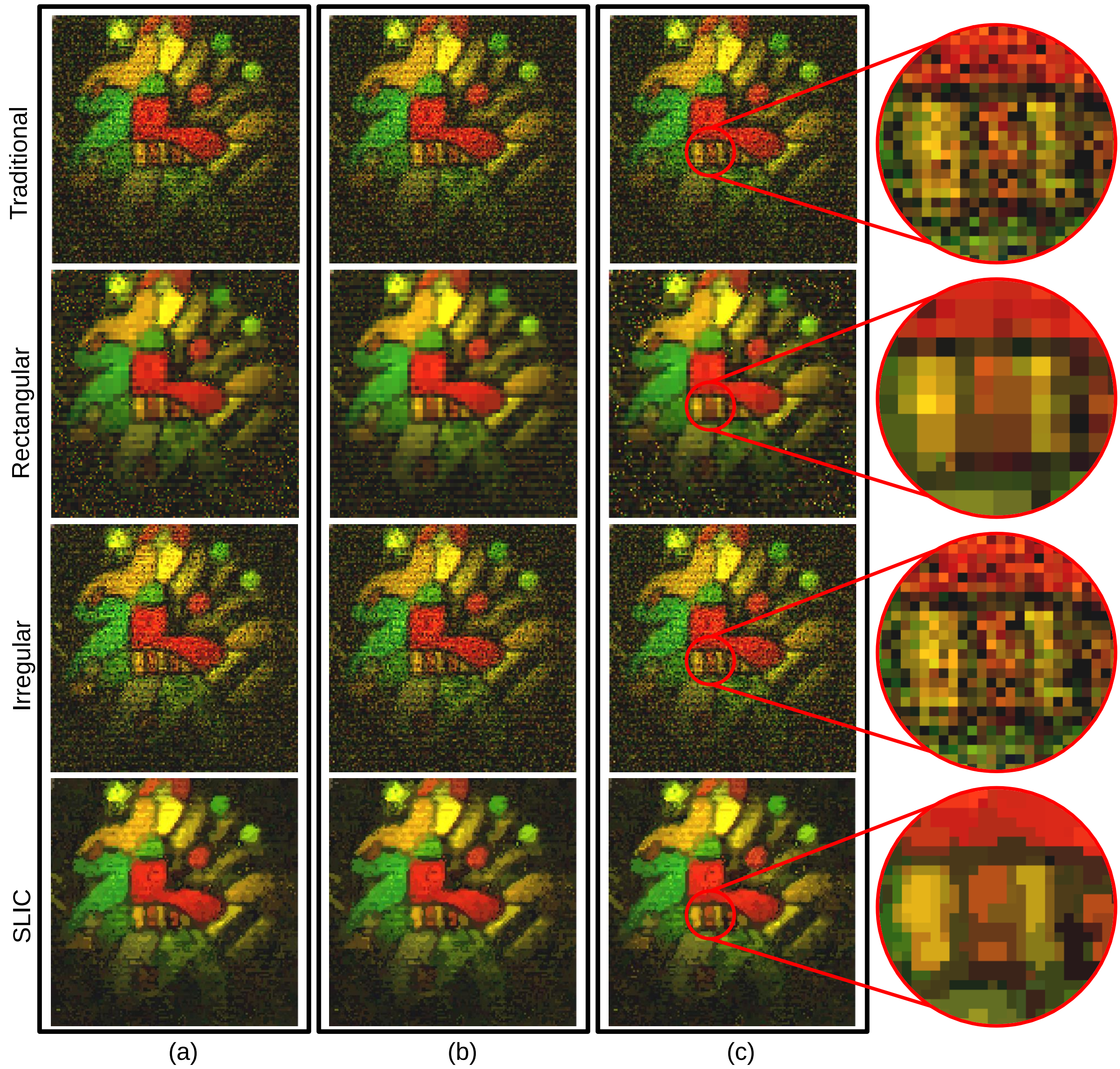

Figure 22: RGB comparison of the reconstructions, using the traditional approach and the proposed MR reconstruction with rectangular, irregular and SLIC super-pixels for $N = 128$, $M = 128$ and (a)$L = 30$ (b) $L = 90$ and (c)$L = 200$.

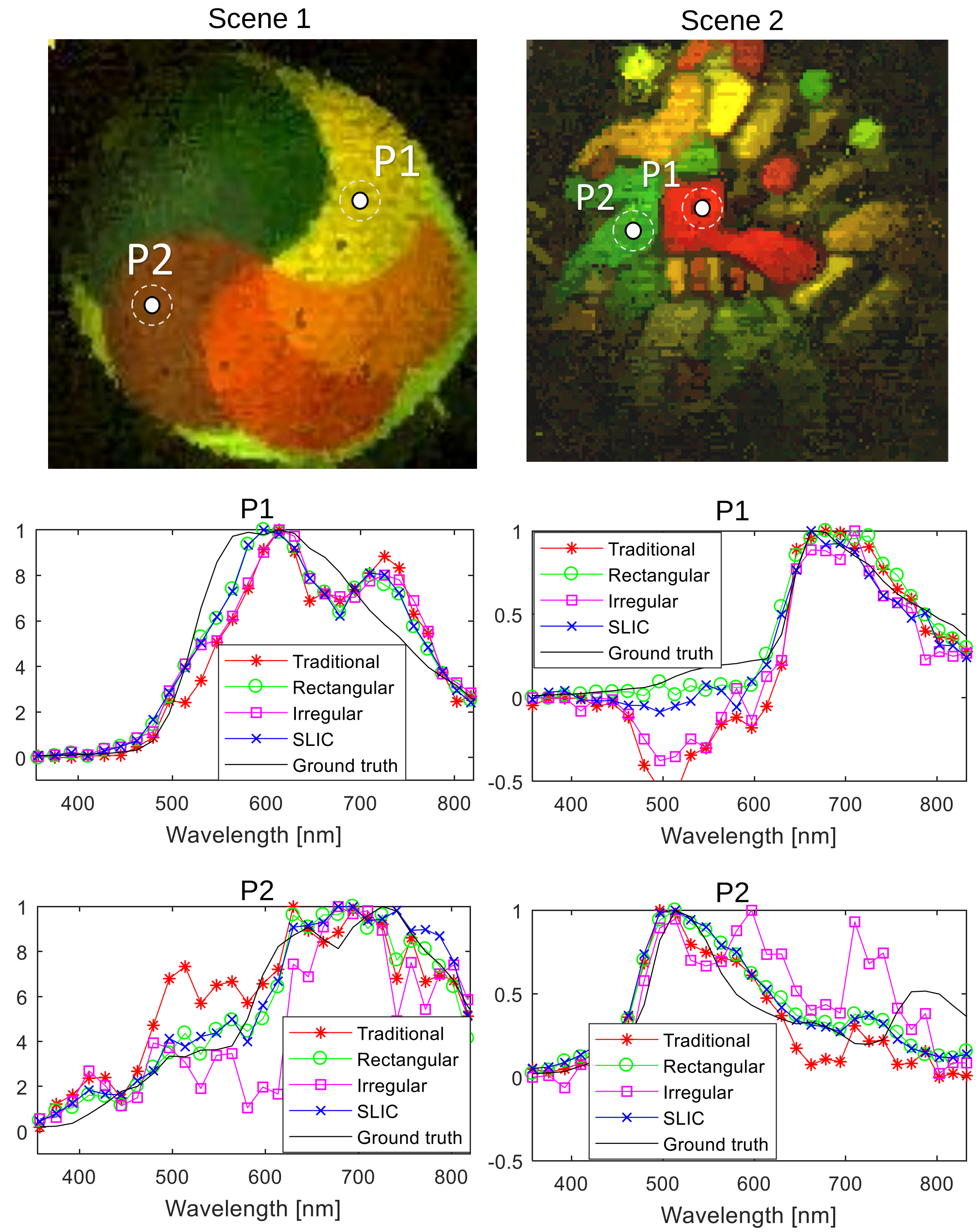

Figure 23: Comparison of the spectral signatures of the two recovered scenes, with $L = 30$ using the traditional reconstruction approach and different types of super-pixels proposed in this paper.

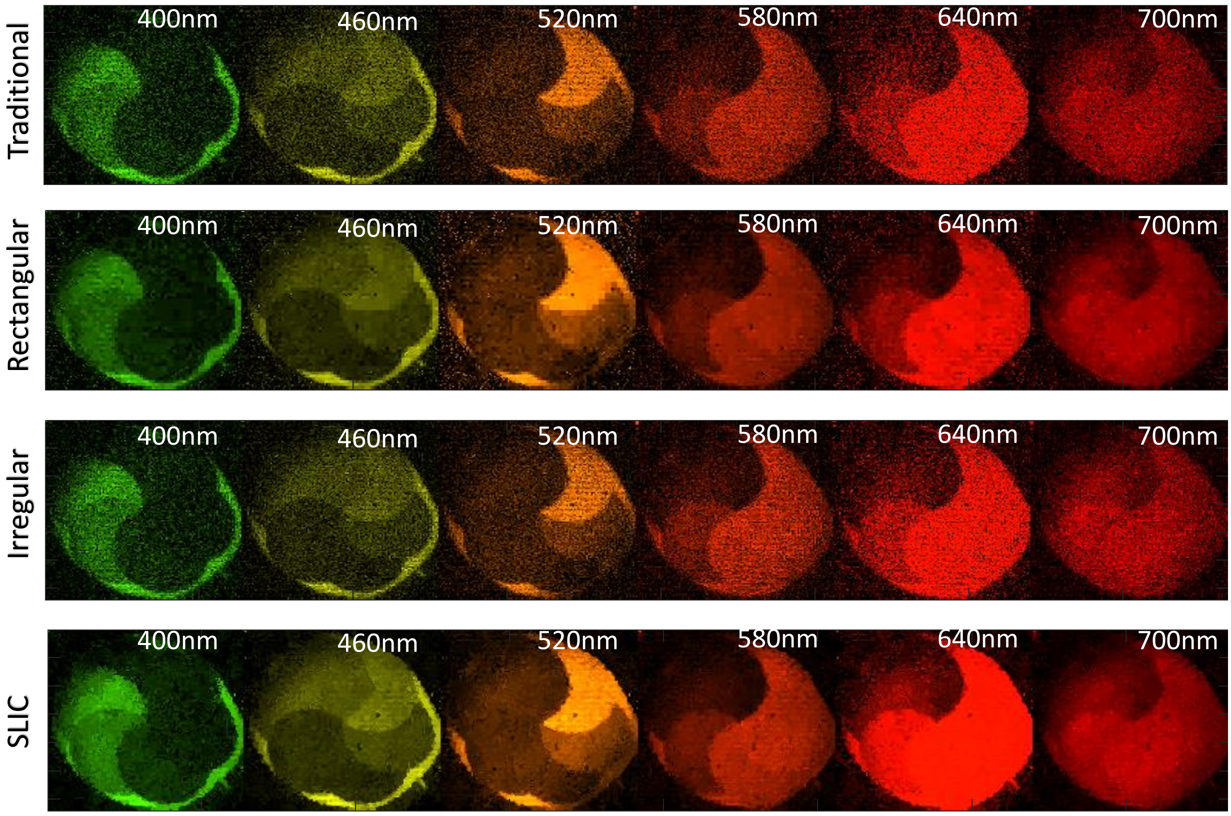

Figure 24: Comparison of 6 spectral bands between the reconstruction approaches for fist real scene, with $M = N = 128$, $L = 30$.

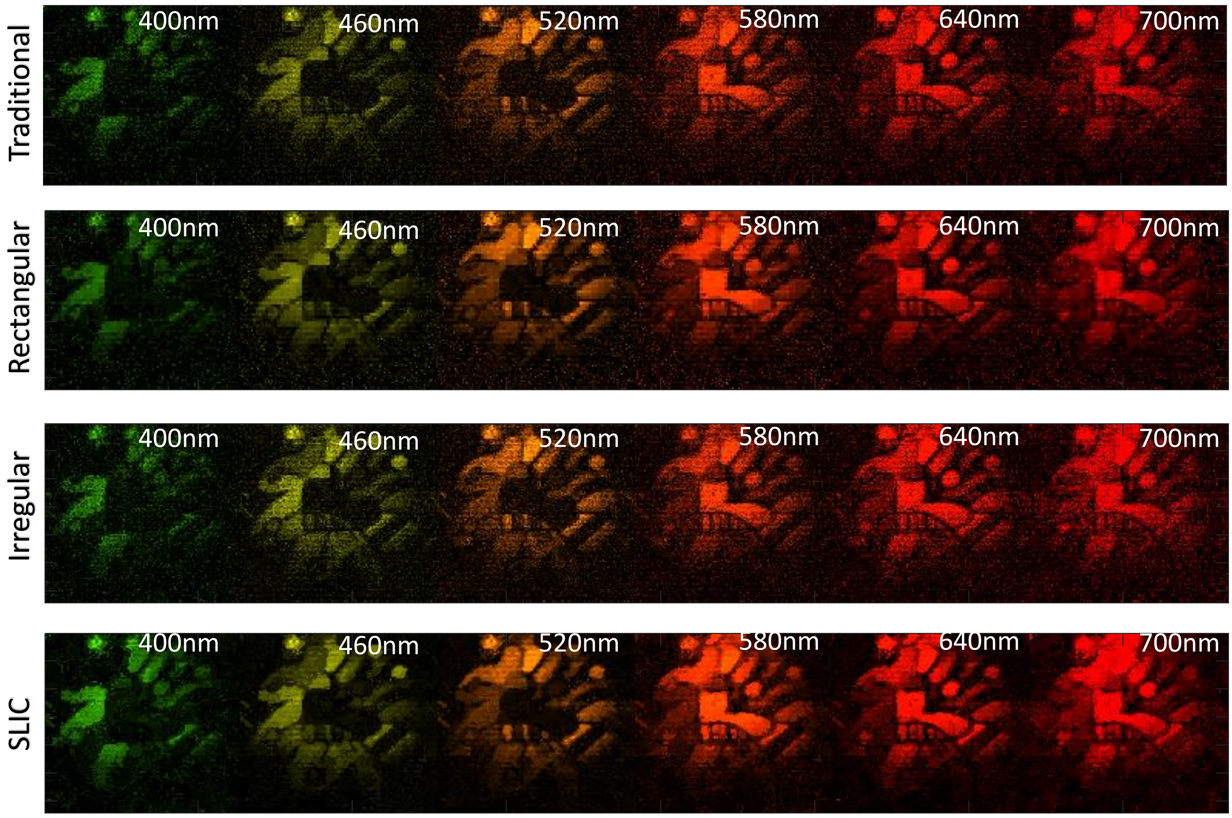

Figure 25: Comparison of 6 spectral bands between the reconstruction approaches for second real scene, with $M = N = 128$, $L = 30$.

Chapter 6

Conclusions

- A mathematical model for the compressive spectral imaging acquisition process with a single pixel camera has been developed.
- A mathematical model to recover full-resolution spectral signals measured by the single pixel architecture has been developed.
- A mathematical model for the multi-resolution reconstruction of spectral images from single pixel measurements has been proposed.
- The proposed MR reconstruction approach includes three different types of super-pixels: rectangular, irregular, and based on SLIC.
- Simulation and experimental results show that the proposed methods provide accurate and faster spatial and spectral reconstructions when compared to the traditional full resolution reconstruction approach, with improvements of up to 6dB, 5dB and 6dB of PSNR for the irregular, rectangular, and SLIC super-pixels, respectively.
- Using the irregular super-pixels results in an improvement of up to 0.38 of SSIM, for the rectangular super-pixels an improvement of up to 0.24, and for the SLIC super-pixels an improvement of up to 0.30 is attained.
- Results show that the proposed MR approach is faster than the traditional approach, independently of the employed super-pixel type (rectangular, irregular, SLIC).

References

[1] X. Lin, Y. Liu, J. Wu, and Q. Dai, "Spatial-spectral encoded compressive hyperspectral imaging," *ACM Trans. Graph.*, vol. 33, no. 6, pp. 233:1–233:11, 2014.

[2] A. Wagadarikar, R. John, R. Willett, and D. Brady, "Single disperser design for coded aperture snapshot spectral imaging," *Appl. Opt.*, vol. 47, no. 10, pp. B44–B51, 2008.

[3] X. Lin, G. Wetzstein, Y. Liu, and Q. Dai, "Dual-Coded Compressive Hyper-Spectral Imaging," *Classical Optics 2014, OSA Technical Digest (online) (Optical Society of America, 2014)*, vol. 39, no. 7, pp. 2044–2047, 2014.

[4] X. Cao, H. Du, X. Tong, Q. Dai, and S. Lin, "A prism-mask system for multispectral video acquisition," *IEEE Transactions on Pattern Analysis and Machine Intelligence*, vol. 33, no. 12, pp. 2423–2435, 2011.

[5] M. Duarte, M. Davenport, D. Takhar, J. Laska, T. S. T. Sun, K. Kelly, and R. Baraniuk, "Single-Pixel Imaging via Compressive Sampling," *IEEE Signal Processing Magazine*, vol. 25, no. 2, pp. 1–19, 2008.

[6] H. B. GA Shaw, "Spectral Imaging for Remote sensing," *Lincoln Laboratory Journal*, vol. 14, no. 1, pp. 3–28, 2003.

[7] G. Lu and B. Fei, "Medical hyperspectral imaging: a review," *Journal of biomedical optics*, vol. 19, no. 1, p. 10901, 2014.

[8] C. M. Stellman, F. M. Olchowski, and J. V. Michalowicz, "WAR HORSE (wide-area reconnaissance: hyperspectral overhead real-time surveillance experiment)," pp. 339–346, 2001.

[9] D. L. Donoho, "Compressed sensing," *IEEE Transactions on Information Theory*, vol. 52, no. 4, pp. 1289–1306, 2006.

[10] D. Takhar, J. N. Laska, M. B. Wakin, M. F. Duarte, D. Baron, S. Sarvotham, K. F. Kelly, and R. G. Baraniuk, "A new compressive imaging camera architecture using

optical-domain compression," *Proceedings of SPIE*, vol. 6065, pp. 606 509–606 509–10, 2006.

[11] Y. August, C. Vachman, Y. Rivenson, and A. Stern, "Compressive hyperspectral imaging by random separable projections in both the spatial and the spectral domains," *Applied optics*, vol. 52, no. 10, pp. D46–54, 2013.

[12] Y. Rivenson and A. Stern, "Compressed imaging with a separable sensing operator," *IEEE Signal Processing Letters*, vol. 16, no. 6, pp. 449–452, 2009.

[13] Y. Fang, L. Chen, J. Wu, and B. Huang, "GPU Implementation of Orthogonal Matching Pursuit for Compressive Sensing," *2011 IEEE 17th International Conference on Parallel and Distributed Systems*, pp. 1044–1047, 2011.

[14] H. Arguello, C. V. Correa, and G. R. Arce, "Fast lapped block reconstructions in compressive spectral imaging," *Appl. Opt.*, vol. 52, no. 10, pp. D32—-D45, 2013.

[15] A. Roman-Gonzalez and N. I. Vargas-Cuentas, "Análisis de imágenes hiperespectrales Hyperspectral images analysis," *Revista Ingenieria & Desarrollo*, vol. 35, pp. 14–17, 2014.

[16] R. O. Green, M. L. Eastwood, C. M. Sarture, T. G. Chrien, M. Aronsson, B. J. Chippendale, J. A. Faust, B. E. Pavri, C. J. Chovit, M. Solis, M. R. Olah, and O. Williams, "Imaging spectroscopy and the Airborne Visible/Infrared Imaging Spectrometer (AVIRIS)," *Remote Sensing of Environment*, vol. 65, no. 3, pp. 227–248, 1998.

[17] P. Mouroulis and M. M. McKerns, "Pushbroom imaging spectrometer with high spectroscopic data fidelity: experimental demonstration," *Optical Engineering*, vol. 39, no. 3, pp. 808–816, 2000.

[18] A. Jerri, "The Shannon Sampling Theorem - its various extensions and application: ATutorial Review," 1977.

[19] H. J. Landau, "Sampling, data transmission, and the Nyquist rate," *Proceedings of the IEEE*, vol. 55, no. 10, pp. 1701–1706, 1967.

[20] R. Baraniuk, "Compressive Sensing [Lecture Notes]," *IEEE Signal Processing Magazine*, vol. 24, no. July, pp. 118–121, 2007.

[21] H. Arguello, Y. Wu, H. Rueda, W. Prather, and G. Arce, "Higher-order computational model for coded aperture spectral imaging," *Appl. Opt*, vol. 52, no. 10, pp. D12–D21, 2013.

[22] A. Said and W. A. Pearlman, "An image multiresolution representation for lossless and lossy compression," *IEEE Transactions on Image Processing*, vol. 5, no. 9, pp. 1303–1310, 1996.

[23] Itu-t, "ITU-T Rec. H.265 (10/2014) High efficiency video coding," vol. 265, 2014.

[24] A. Grange and H. Alvestrand, "A VP9 Bitstream Overview," pp. 1–14, 2013.

[25] A. Gonzalez, H. Jiang, G. Huang, and L. Jacques, "Multi-resolution Compressive Sensing Reconstruction," in *2016 IEEE International Conference on Image Processing (ICIP)*, 2016, pp. 1–5.

[26] X. Wang and J. Liang, "Multi-Resolution Compressed Sensing via Approximate Message Passing," *IEEE Transactions on computational imaging*, vol. 2, no. 3, pp. 1–31, 2015.

[27] H. Garcia, Ó. Espitia, and H. Arguello, "Multiresolution Spectral Imaging by Combining Different Sampling Strategies in a Compressive Imager, MR-CASSI," in *XXI symposium on signal processing, images and artificial vision*, Bucaramanga, 2016, p. 6.

[28] A. C. Sankaranarayanan, L. Xu, C. Studer, Y. Li, K. Kelly, and R. G. Baraniuk, "Video Compressive Sensing for Spatial Multiplexing Cameras using Motion-Flow Models," Tech. Rep., 2015.

[29] A. Levinshtein, A. Stere, K. N. Kutulakos, D. J. Fleet, S. J. Dickinson, and K. Siddiqi, "TurboPixels: Fast superpixels using geometric flows," *IEEE Transactions on Pattern Analysis and Machine Intelligence*, vol. 31, no. 12, pp. 2290–2297, 2009.

[30] A. Vedaldi and S. Soatto, "Quick shift and kernel methods for mode seeking," *Lecture Notes in Computer Science (including subseries Lecture Notes in Artificial Intelligence and Lecture Notes in Bioinformatics)*, vol. 5305 LNCS, no. PART 4, pp. 705–718, 2008.

[31] R. Achanta, A. Shaji, K. Smith, A. Lucchi, P. Fua, and S. Sabine, "SLIC Superpixels," Tech. Rep. June, 2010.

[32] R. Achanta, A. Shaji, K. Smith, A. Lucchi, P. Fua, and S. Süsstrunk, "SLIC Superpixels Compared to State-of-the-Art Superpixel Methods," *IEEE Transactions on Pattern Analysis and Machine Intelligence*, vol. 34, no. 11, pp. 2274–2282, 2011.

[33] F. Yasuma, T. Mitsunaga, D. Iso, and S. K. Nayar, "Generalized Assorted Pixel Camera: Postcapture Control of Resolution, Dynamic Range, and Spectrum," *IEEE Transactions on Image Processing*, vol. 19, no. 9, pp. 2241–2253, 2010.

[34] M. A. T. Figueiredo, R. D. Nowak, and S. J. Wright, "Gradient Projections For Sparse Reconstruction: Application to Compressed Sensing and Other Inverse Problems," *J. Selected Topics in Signal Processing, IEEE*, vol. 1, no. 1, pp. 586–598, 2007.

Bibliography

D. L. Donoho, "Compressed sensing", *IEEE Transactions on Information Theory*, vol. 52, no. 4, pp. 1289-1306, 2006.

H. Garcia, O. Espitia, and H. Arguello, "Multiresolution Spectral Imaging by Combining Different Sampling Strategies in a Compressive Imager, MR-CASSI", in *XXI symposium on signal processing, images and artificial vision*, Bucaramanga, 2016, p. 6.

M. Duarte, M. Davenport, D. Takhar, J. Laska, T. S. T. Sun, K. Kelly, and R. Baraniuk, "Single-Pixel Imaging via Compressive Sampling", *IEEE Signal Processing Magazine*, vol. 25, no. 2, pp. 1-19, 2008.

R. Achanta, A. Shaji, K. Smith, A. Lucchi, P. Fua, and S. Susstrunk, "SLIC Superpixels Compared to State-of-the-Art Superpixel Methods", *IEEE Transactions on Pattern Analysis and Machine Intelligence*, vol. 34, no. 11, pp. 2274-2282, 2011.

R. Baraniuk, "Compressive Sensing [Lecture Notes]", *IEEE Signal Processing Magazine*, vol. 24, no. July, pp. 118-121, 2007.

X. Wang and J. Liang, "Multi-Resolution Compressed Sensing via Approximate Message Passing", *IEEE Transactions on computational imaging*, vol. 2, no. 3, pp. 1-31,2015.